



Buss, H. L., Chapela Lara, M., Moore, O. W., Kurtz, A. C., Schulz, M. S., & White, A. F. (2017). Lithological influences on contemporary and long-term regolith weathering at the Luquillo Critical Zone Observatory. *Geochimica et Cosmochimica Acta*, 196, 224-251.
<https://doi.org/10.1016/j.gca.2016.09.038>

Peer reviewed version

License (if available):
CC BY-NC-ND

Link to published version (if available):
[10.1016/j.gca.2016.09.038](https://doi.org/10.1016/j.gca.2016.09.038)

[Link to publication record in Explore Bristol Research](#)
PDF-document

This is the author accepted manuscript (AAM). The final published version (version of record) is available online via Elsevier at <http://www.sciencedirect.com/science/article/pii/S0016703716305634>. Please refer to any applicable terms of use of the publisher.

University of Bristol - Explore Bristol Research

General rights

This document is made available in accordance with publisher policies. Please cite only the published version using the reference above. Full terms of use are available:
<http://www.bristol.ac.uk/red/research-policy/pure/user-guides/ebr-terms/>

Lithological Influences on Contemporary and Long-Term Regolith Weathering at the Luquillo Critical Zone Observatory

Heather L. Buss^{*a}, María Chapela Lara^a, Oliver W. Moore^a, Andrew C. Kurtz^c, Marjorie S. Schulz^b, Art F. White^b

^a School of Earth Sciences, University of Bristol, Wills Memorial Building, Queens Road, Bristol BS8 1RJ, UK

^b U.S. Geological Survey, 325 Middlefield Rd., MS-420, Menlo Park, CA 95025, USA

^c Department of Earth and Environment, Boston University Boston, MA 02215, USA

* Corresponding author: h.buss@bristol.ac.uk,

Tel: +44(0)117 33 14751, Fax: +44(0)117 92 53385

Abstract

Lithologic differences give rise to the differential weatherability of the Earth's surface and globally variable silicate weathering fluxes, which provide an important negative feedback on climate over geologic timescales. To isolate the influence of lithology on weathering rates and mechanisms, we compare two nearby catchments in the Luquillo Critical Zone Observatory in Puerto Rico, which have similar climate history, relief and vegetation, but differ in bedrock lithology. Regolith and pore water samples with depth were collected from two ridgetops and at three sites along a slope transect in the volcanoclastic Bisley catchment and compared to existing data from the granitic Río Icacos catchment. The depth variations of solid-state and pore water chemistry and quantitative mineralogy were used to calculate mass transfer (τ) and weathering solute profiles, which in turn were used to determine weathering mechanisms and to estimate weathering rates.

Regolith formed on both lithologies is highly leached of most labile elements, although Mg and K are less depleted in the granitic than in the volcanoclastic profiles, reflecting residual biotite in the granitic regolith not present in the volcanoclastics. Profiles of both lithologies that terminate at bedrock corestones are less weathered at depth, near the rock-regolith interfaces. Mg fluxes in the volcanoclastics derive primarily from dissolution of chlorite near the rock-regolith interface and from dissolution of illite and secondary phases in the upper regolith, whereas in the granitic profile, Mg and K fluxes derive from biotite dissolution. Long-term mineral dissolution rates and weathering fluxes were determined by integrating mass losses over the thickness of solid-state weathering fronts, and are therefore averages over the timescale of regolith development. Resulting long-term dissolution rates for minerals in the volcanoclastic regolith include chlorite: 8.9×10^{-14} mol m⁻² s⁻¹, illite: 2.1×10^{-14} mol m⁻² s⁻¹ and kaolinite: 4.0×10^{-14} mol m⁻² s⁻¹. Long-term weathering fluxes are several orders of magnitude lower in the granitic regolith than in the volcanoclastic, despite higher abundances of several elements in the granitic regolith. Contemporary weathering fluxes were determined from net (rain-corrected) solute profiles and thus represent rates over the residence time of water in the regolith. Contemporary weathering fluxes within the granitic regolith are similar to the long-term fluxes. In contrast, the long-term fluxes are faster than the contemporary fluxes in the volcanoclastic regolith. Contemporary fluxes in the granitic regolith are generally also slightly faster than in the volcanoclastic. The differences in weathering fluxes over space and time between these two watersheds indicate significant lithologic control of chemical weathering mechanisms and rates.

Keywords: chemical weathering, critical zone, regolith, saprolite, soil formation

1. INTRODUCTION

Silicate mineral weathering in the critical zone is a primary source of solutes and sediments to streams and oceans where they contribute to the sequestration of CO₂, providing a negative climate feedback over geologic time (e.g., Berner and Berner, 1997). Therefore, the relative weatherability of Earth's surface (e.g., Kump et al., 2000) is a fundamental constraint on Earth's climate as well as on biogeochemical cycles. Relative weatherability and the lithologic mechanisms that produce silicate weathering products can only be identified and isolated by comparing weathering of different rock types while controlling for climate variability and other parameters (e.g., Berner, 2008). However, many previous studies of silicate weathering fluxes have not controlled for climate in this way (e.g., Bluth and Kump, 1994; White and Blum, 1995; Kump et al., 2000; Dessert et al., 2001).

Silicate weathering also provides mineral nutrients to soils and regolith and is an important factor in the rate of regolith formation and evolution. It is likely that the majority of exported solutes are liberated by weathering processes occurring deep in the critical zone (e.g., Rad et al., 2007; Kurtz et al., 2011; Schopka and Derry, 2012) where weathering-susceptible primary minerals are abundant and exposed to reactive fluids: at rock-regolith interfaces or within bedrock aquifers and fracture networks near the water table. Weathering at rock-regolith interfaces produces porosity and essential mineral nutrients (e.g., P, Mg, Ca, K, Fe), which support terrestrial ecosystems (Walker and Syers, 1976; Buss et al., 2005; 2008; 2010; Graham et al., 2010; Minyard et al., 2011; Hahm et al., 2014). Although near-surface and deep critical zone ecosystems may operate as largely independent nutrient cycles (Buss et al., 2005), especially in deep tropical regolith, they may still affect one another because *i*) regolith formed at the rock-regolith interface will effectively move towards the surface as erosion lowers the ground surface over time (e.g., Brantley and White, 2009) and *ii*) weathering reactions and soil organisms can alter the chemistry and reactivity of infiltrating water. For example, respiration of O₂ by soil microorganisms reduces the concentration of O₂ in pore water, which can slow down both geochemical and biological oxidation reactions (Fletcher et al., 2006; Buss et al., 2008; Bazilevskaya et al., 2013; Brantley et al., 2014).

In *in situ* critical zones, the link between the near-surface (classical soil) and deep zones (fractured and disaggregating bedrock) is saprolite. Here we use the term *saprolite* to refer to friable material weathered in place (not strictly limited to isovolumetrically weathered material), *soil* for the overlying, bioturbated, rooting zone and *regolith* as a general term encompassing soil, saprolite and any mobile, weathered, friable material (e.g., Taylor and Eggleton, 2001). Mineral weathering and biogeochemical processes within saprolite determine many characteristics of the overlying soil; indeed, saprolite has traditionally been considered parent material, or C-horizon, in classical soil science (Richter and Markewitz, 1995). Furthermore, as noted above, mineral weathering and

biogeochemical processes within regolith also determine the reactivity of pore water that reaches the underlying bedrock, with implications for whole-rock weathering rates, regolith formation rates, watershed solute fluxes, and modulation of global CO₂. Mineral weathering reactions within regolith also produce nutrients and energy sources for resident microorganisms (e.g., Buss et al., 2005).

Despite the importance of silicate mineral weathering rates to myriad critical zone and global processes, relatively few field-based rates have been measured (see compilation in White and Buss, 2014) and most weathering studies of volcanic materials have focused on basaltic terrains. Different lithologies have different mineral assemblages and different characteristics (e.g., grain size) that may affect mineral weathering mechanisms and rates. Although andesite and basalt make up similar proportions of the global land surface, andesites are more common on tropical and subtropical islands and near active margins while many of the basaltic terrains worldwide are located on continents and at higher latitudes. Tropical watersheds, which cover only about 25% of the terrestrial surface, produce 65% of the dissolved silica flux to the oceans via mineral weathering processes (Stallard and Edmond, 1983; Meybeck, 1987). Volcanic islands, globally, contribute about 30% of the solute flux to the world's oceans despite representing only 9% of the terrestrial surface (Rad et al., 2007). Therefore, silicate weathering fluxes from low-latitude andesites may be more significant to global CO₂ consumption than fluxes from basalts (Goldsmith et al., 2010). However, measured watershed-scale silicate weathering fluxes in andesitic and basaltic watersheds are similar (McDowell and Asbury, 1994; Dessert et al., 2003 and references therein; Rad et al., 2006; Goldsmith et al., 2008; 2010).

The aforementioned andesitic weathering studies determined chemical weathering fluxes from concentration and discharge data for rivers draining catchments of interest, effectively providing watershed-averaged, endpoint views of chemical weathering from which weathering mechanisms and rates are inferred. That approach is complemented by studies that examine chemical weathering processes within weathering profiles, i.e., *in situ*, which provide mechanistic information enabling determination of mineral-specific reaction rates (Brantley and White, 2009; White and Buss, 2014) as well as providing spatially resolved information about mineral nutrient availability in terrestrial ecosystems (e.g., Buss et al., 2005). Several studies of both types have been done in the Luquillo Mountains of Puerto Rico, in what is now the Luquillo Critical Zone Observatory (LCZO) (McDowell and Asbury, 1994; Murphy et al., 1998; White et al., 1998; Schulz and White, 1999; Buss et al., 2008; 2010; Stallard, 2012; Buss et al., 2013), mostly within the granitic Río Icacos watershed. Here we present weathering profile data from the andesitic, meta-volcaniclastic Bisley catchment as a comparison to the neighboring granitic Río Icacos catchment to investigate the influence of lithology on regolith weathering processes and rates, and on mineral nutrient

104 availability. Solid-state elemental and mineral abundances with depth in the regolith were used to
105 estimate mineral weathering rates and elemental fluxes over the timescale of regolith development
106 (*long-term rates*). Such calculations, from White (2002), assume that a linear approximation of the
107 gradient of the weathering front (depth-dependent depletion of a mobile element or weathering
108 mineral) represents the sum of two vectors: the whole-rock weathering advance rate and the
109 element- or mineral-specific weathering rate. Similarly, solute profiles were used to estimate
110 elemental weathering fluxes on the timescale of water infiltration into the regolith (*contemporary*
111 *rates*); in this case the gradient results from vectors representing the hydraulic flux and the element-
112 specific weathering flux.

113

114

2. FIELD SITE

115 The Luquillo Mountains in northeastern Puerto Rico are characterized by steep, rugged topography,
116 highly dissected valleys, a hot and humid climate, thick regolith, and dense, tropical vegetation. The
117 Luquillo Mountains host the 113 km² Luquillo Experimental Forest (LEF), a forest preserve
118 administered by the U.S. Forest Service that has been designated an International Biosphere
119 Reserve by UNESCO and hosts the U.S. Geological Survey (USGS) Luquillo Water Energy and
120 Biogeochemical Budgets (WEBB) project, a National Science Foundation (NSF) long-term
121 ecological research site (Luq-LTER) and a NSF critical zone observatory (LCZO). Several large
122 river systems drain the Luquillo Mountains north to the Atlantic Ocean (Río Mameyes, Río Sabana,
123 Río Espíritu Santo, and Río Fajardo) or south to the Caribbean Sea (Río Blanco).

124 The Bisley experimental watersheds are a sequence of 5 adjacent, small catchments
125 (numbered 1-5, from east to west) that feed the Río Mameyes. Elevation in the 44 km² (17.8 km²
126 gaged area) Río Mameyes watershed ranges from 80 to 1050 m. In the Bisley watersheds, elevation
127 ranges from 260-400 m. Mean monthly temperatures in the Bisley watersheds are relatively
128 constant, fluctuating seasonally by about 3-4°C, with winters averaging about 24°C and summers
129 about 27.5°C (Schellekens, et al., 2004; NWS, 2007). Rainfall increases with altitude in the
130 Luquillo Mountains, from about 2500 to 4500 mm y⁻¹ over 1200 m of altitude (Garcia-Martino et
131 al., 1996). The Bisley watersheds typically receive 3000-4000 mm y⁻¹ of rainfall (Scatena, 1989),
132 largely delivered in short, but intense, storm events. Mean annual runoff from 1991-2005 was 3760
133 mm y⁻¹ in the Río Icacos and 2750 mm y⁻¹ in the Río Mameyes (Murphy and Stallard, 2012).
134 Mineral aerosol dust from Africa contributes significant nutrients to the Caribbean islands; P flux
135 from dust was estimated at 210 ± 70 kg ha⁻¹ y⁻¹ to the Río Icacos watershed (Pett-Ridge, 2009) and
136 dust is estimated to account for 0-8% of shallow ridgetop soils across the LCZO (McClintock et al.,
137 2015).

138 The Bisley watersheds are underlain by the ~100 Ma, basaltic to andesitic, marine-bedded
139 meta-volcaniclastic Fajardo Formation (Jolly et al., 1998), formed from a near-sea level volcanic
140 complex that produced pyroclastic debris that was deposited in the sea after transport and reworking
141 (Seiders 1971). The Fajardo Formation underwent contact metamorphism during the intrusion of
142 the nearby Río Blanco Quartz Diorite stock (actually a tonalite according to the current IUGS
143 classification scheme), as evidenced by the mineral assemblages (Buss et al., 2013), and is
144 comprised of several units including an upper thin-bedded tuffaceous siltstone and sandstone, an
145 upper thick-bedded tuff, a lower thin-bedded tuffaceous sandstone and siltstone, a lower thick-
146 bedded tuff, and an undivided unit (Briggs, 1973; Briggs and Aguilar-Cortes, 1980). Bed
147 thicknesses vary and coarse tuff, breccias, and cherty or calcareous siltstone beds are found in some
148 units. Although the bedrock exposures in the Bisley watersheds appear homogeneous, the
149 catchment is underlain by the upper thick-bedded tuff unit, which includes some breccias, lithic
150 andesitic clasts, calcareous siltstone, and some pumice and red scoria (Briggs and Aguilar-Cortes,
151 1980). The grain size and color of bedrock samples vary slightly within the Bisley watershed, but
152 the elemental composition is not highly variable (Buss et al., 2013). For simplicity and consistency
153 with other published studies from this site, we refer to the Bisley bedrock as “volcaniclastic” and
154 the intrusion bedrock as “granitic” throughout the manuscript.

155 Ridges in the Bisley watersheds are mantled by thick (9 to 15+ m), highly cohesive regolith.
156 Landslides, soil creep, and tree throws incise and sharpen the ridges, and leave high angle slopes (in
157 Bisley 1 and 2, over 50% of the area has slopes > 45° and 15% of the slopes are > 70°; Scatena,
158 1989) with thinner regolith (~1 to 3 m). By area, Bisley 1 and 2 are about 17% ridges and 65%
159 slopes (Scatena et al., 1993). Some slopes, lower elevation ridges, and valleys are riddled with
160 boulders. The Bisley 1 ridgetop soils are Ultisols of the Humatas Series, which are 0.8-1.0 m deep,
161 moderately well-drained, very-fine, parasesquic, isohyperthermic Typic Haplohumults (Scatena,
162 1989; Silver et al., 1994; USDA NCRS, 2002). Biomass in the Bisley watersheds (Scatena et al.,
163 1993) is dominated by Tabonuco trees (*Dacryodes excelsa*), which make up 45.7% of the
164 aboveground biomass in the Bisley 1 and 2 watersheds. Non-seedling trees (>2.5 cm diameter at 1.3
165 m height) and coarse roots (>0.5 cm) make up 73.5 and 24.1% of vegetation biomass, respectively,
166 in Bisley 1 and 2. Ridges contain the highest aboveground biomass per unit area compared to other
167 topographic categories (Scatena et al., 1993). Sierra palm trees (*Prestoea acuminata*) and ferns are
168 also common, particularly in the valleys. Soil is mantled by a thin layer of leaf litter in most areas.

169

170

3. METHODS

171 Regolith cores, approximately 10 cm diameter, were collected by hand-augering to the point of
172 refusal at 5 sites (Fig. 1) in the Bisley 1 catchment. Two of the sites, B1R and B1S1, are located on
173 *cuchillos* (knife-edge ridges). Site B1R is located at N18° 18.831, W65° 44.567 (NAD83), at about
174 400 masl (near the top of a north-south striking ridge), along the drainage divide between the Bisley
175 1 stream (a tributary of the Río Mameyes) and the Río Sabana. Both of these river (*río*) systems
176 drain north to the Atlantic Ocean. Site B1S1 is located at N18° 18.956, W65° 44.700, at about 285
177 masl and is 330 m northwest of site B1R on a ridge about 55 m northeast and 50 m above the Bisley
178 1 stream gage. Sites B1S2, B1S3, and B1S4 are located along the slope (approximate elevations:
179 280, 275, and 268 masl, respectively) between ridgetop site B1S1 and the Bisley 1 stream (Fig. 1).
180 Site B1S4 (N18° 18.937, W65° 44.711) is located within the floodplain of the Bisley 1 stream. The
181 deepest regolith core from each site was collected for analysis, but numerous holes were augered in
182 the course of installing pore water and gas samplers. Additional holes were augered at several
183 points along the length of the B1R ridge, between the top (where the site is located) and about 440
184 m north. Partially weathered rock fragments were collected during augering and from saprolite
185 outcrops along the road. Soil pits were dug at sites B1R and B1S1 to examine the soil texture and
186 appearance. Bedrock samples were collected from exposed corestones and from two boreholes
187 drilled to 27.0 and 37.2 m depth near the Bisley 1 stream gage as reported in Buss et al. (2013).

188 Vadoses zone pore waters were collected from 5 cm diameter nested porous-cup suction water
189 samplers (Soil Moisture Inc, Santa Barbara, CA) that were installed in hand-augered holes at depths
190 from 0.15 to 16.0 m at the 5 Bisley sites. The depth to auger refusal at the B1S(1-4) sites was 9.3,
191 2.7, 1.5 and 0.9 m, respectively. Augering at B1R was halted at 16 m depth without reaching auger
192 refusal. Pore water samplers were left under approximately 80 cbars vacuum and the pore waters
193 were collected approximately monthly from January 2007 – September 2008 at site B1R and from
194 January 2008 – November 2009 at sites B1S(1-4). Openfall precipitation (wet + dry deposition) was
195 measured and sampled monthly from a collector situated on an observation tower near site B1R,
196 above the forest canopy.

197 Regolith gas samplers (3.2 mm stainless steel tubing tipped with stainless steel mesh) were
198 bundled and installed in hand augered holes at sites B1R and B1S1 in Bisley and site LG1 in Río
199 Icacos. Although gas samplers were installed and sampled by the USGS at LG1 in the 1990's
200 (White et al., 1998), degradation of those samplers and later improvements to the sampler design
201 and collection methodology prompted us to install new equipment. The screened openings were
202 packed in quartz sand at depth intervals separated by bentonite plugs and native regolith. Gas tubes
203 were purged using a plastic syringe prior to sampling. Samples were taken with a gas-tight
204 apparatus attached to a needle and collected in septa-sealed gas canisters under vacuum, which were

205 shipped to the USGS in Menlo Park for measurement of O₂ and CO₂ by gas chromatography (GC).
206 Sampling canisters were deemed airtight as standards were also transported to and from Puerto Rico
207 in sampling canisters and were still accurate when analysed by GC upon return.

208 Gravimetric water content of the regolith was measured by weighing augered samples, stored
209 in airtight containers, before and after air-drying. Bulk densities were determined from samples
210 collected with a hand soil corer with removable internal rings of known volume (Soil Moisture,
211 Santa Barbara) to depths of 5.0 and 6.7 m at sites B1R and B1S1, respectively. Density
212 measurements excluded samples with cobbles and large pebble-sized rock fragments.

213 Bulk solid-state chemical analysis was performed on pulverized and sieved (150 µm) rock,
214 weathered rock fragments, and regolith samples. Regolith samples were sieved to 2 mm prior to
215 pulverization. Solid samples were digested by lithium metaborate fusion and major and minor
216 elements (Al, Ca, Cr, Fe, K, Mg, Mn, Na, P, Si, Ti, Ba, Sr, Zn, Zr) were determined by ICP-AES,
217 and FeO was determined by titration after multi-acid digest (SGS Mineral Laboratories, Ontario,
218 Canada). Splits of some solid samples were dissolved in a multi-acid digest (HF, HCl, HNO₃) and
219 also analyzed via ICP-MS at the USGS (Menlo Park, CA) for comparison. Exchangeable cations
220 were estimated by ICP-MS analysis (USGS, Menlo Park, CA) of NH₄-acetate extracts of regolith
221 samples. Briefly, regolith samples (5 g) were extracted in 100 ml of un-buffered 0.1 N NH₄-acetate.
222 Samples were shaken for one hour and allowed to settle overnight. Supernatants were removed with
223 a syringe and filtered to 0.45 µm (SFCA-membrane, Cole-Parmer).

224 Pore waters from the suction samplers and precipitation samples were filtered in the
225 laboratory and the pH and alkalinity were measured on some pore waters. Water samples were
226 analyzed by ion chromatography (IC) for anions and ICP-MS for cations (both at the USGS in
227 Menlo Park, CA). Elemental concentrations in precipitation samples were volume-averaged.

228 Thin sections were prepared from rock, weathered rock fragments, and regolith samples
229 (Vancouver Petrographics, Canada and Spectrum Petrographics, Vancouver, WA, USA). Scanning
230 electron microscopy (SEM) in backscattered electron mode with energy dispersive spectrometry
231 (EDS) were performed on thin sections at the USGS (Menlo Park, CA, USA) and at the University
232 of Bristol. Powder X-ray diffraction was performed at the USGS (Boulder, CO, USA), using a
233 Siemens D500 diffractometer. Quantitative mineral abundances were determined from powder X-
234 ray diffraction data by whole-pattern fitting using the computer program ROCKJOCK (Eberl, 2003)
235 and compared to bulk chemical abundances using HANDLENS (Eberl, 2008). Sample preparation
236 for quantitative analysis was performed as described in Eberl (2003).

237 Solid and solute data for the ridgetop site LG1 in the granitic Río Icacos watershed from Buss
 238 et al. (2005), White (2002), White et al. (1998) and Schulz and White (1999) are presented as
 239 comparison to the ridgetop sites B1S1 and B1R in the volcaniclastic Bisley watershed.
 240 Uncertainties presented for all data were estimated as either the detection limits of the analytical
 241 method (mineralogy by XRD, elemental chemistry by ICP-AES, ICP-MS or IC), laboratory
 242 repeatability (moisture content, bulk density) or the standard error (SE) of the means for the
 243 averaged datasets (compositions of rainfall, pore waters and pore gases sampled over time and of
 244 bedrock sampled at different locations). We present SE for all averaged data to indicate the
 245 statistical accuracy of the averages, because we later use these averages to calculate average mass
 246 transfer, average elemental fluxes and average mineral weathering rates over annual (or longer)
 247 timescales. Therefore, in this context, SE is more appropriate than standard deviations (SD), which
 248 reflect the scatter in the data used in the averages (e.g., month-to-month pore water chemistry).
 249 Uncertainties presented for all calculated values were fully propagated from the aforementioned
 250 uncertainties on the contributing datasets using standard error propagation rules.

251

252 4. RESULTS

253 4.1. Physical Observations and Measurements

254 Visibly unweathered rock samples recovered from the boreholes and the stream beds are fine- to
 255 medium fine-grained, dark blueish or greenish grey. Augered cores and soil pits reveal
 256 hydraulically unsaturated, fine-grained regolith that is red to orange in color except for some grey
 257 mottling at ~1.0 to 1.5 m depth. An exception is site B1S4, located in the floodplain of the Bisley 1
 258 stream, which was saturated and entirely grey in color. We were unable to reach bedrock by hand-
 259 augering at site B1R and stopped at 16 m after 4 days. Site B1S3 is located on a narrow flat
 260 produced by the roots of a fallen tree and as such should be regarded as physically disturbed.
 261 Occasional, small weathered clasts were recovered from the auger at all sites. Relict mineral grains
 262 and thin, linear, black Mn-oxide and white clay zones are visible in the regolith.

263 Bedrock density is 2.3 g cm^{-3} , measured by volume displacement. Dry bulk density of the
 264 regolith generally increases with depth in the soil, then decreases slightly in the underlying regolith
 265 (Table 1). B1R soils and regolith are slightly denser than B1S1. Porosity is estimated from dry bulk
 266 density ρ and specific density ρ_s (the density of soil solids, commonly assumed to be 2.65 g cm^{-1}) as
 267 shown:

$$268 \quad \theta = 100 \left(1 - \frac{\rho}{\rho_s} \right) \quad (1).$$

269 Average estimated porosity and % water content by mass (Table 1) are higher in B1S1 regolith
270 (60% and 30% respectively) than in B1R regolith (46% and 20%, respectively).

271 **4.2. Chemistry**

272 *4.2.1. Solid-State Chemistry*

273 Regolith samples are significantly depleted in base cations (Table 2). Ferrous iron, measured at site
274 B1R only, was very low (≤ 0.2 wt %) within the soil (approx. 0-1.0 m depth) and below detection
275 (< 0.1 wt%) at all depths below 1 m. Solid state elemental concentrations are more variable with
276 depth at site B1R than at the other sites, with no discernible trend in most elements. In contrast,
277 solid-state concentrations with depth at sites B1S(1-4) generally follow expected trends with mobile
278 cations (e.g., Mg, K) increasing with depth and relatively immobile cations (Al, Si, Fe, Ti, Zr)
279 remaining approximately constant or decreasing with depth. Na and Ca are very low or below
280 detection in most samples at all sites, but Ca shows an increase with depth at site B1S4. Manganese
281 increases with depth at site B1S1.

282 Total extractable cation content of the regolith is very low: about 0.5 meq/100g at the surface
283 of B1S1, increasing with depth to 2.7 meq/100g at 9.3 m. The B1R regolith extractable cation
284 content is even lower, measuring below about 0.5 meq/100g except in the upper soil layer.
285 Extractable cations are dominated by Mg in both profiles and make up $\leq 10\%$ of the total Ca in the
286 bulk regolith, $\leq 8\%$ of the total Mg, $\leq 4\%$ of the total K and $\leq 14\%$ of the total Na (Table 3).

287 *4.2.2. Solute Chemistry*

288 Average pore water compositions for the most abundant elements (and Sr) are shown in Table
289 4. Pore water solutes were dominated by Si and Na at all sites. The predominance of pore water
290 cations at the B1S(1-4) and B1R sites generally decreases in the order $\text{Na} > \text{Si} > \text{Mg} > \text{Ca} \geq \text{K} > \text{Al}$
291 $> \text{Mn} > \text{Ba} \approx \text{Sr} > \text{Rb}$, with Fe below detection in most samples. Silicon concentrations were high
292 at the surface, decreasing with depth in the soil layer (upper 1.0-1.5 m), then increasing with depth
293 in the saprolite at all Bisley sites (Fig. 2). Average anion concentrations in the pore waters generally
294 decrease in the order $\text{Cl} \gg \text{SO}_4 \approx \text{NO}_3 > \text{Br} > \text{F}$. Fluoride was below detection in most samples and
295 NO_3 exceeds SO_4 in a number of samples. Phosphorus was below detection in all pore water
296 samples.

297 *4.2.3 Soil gas compositions and pH distributions*

298 Measured pH of pore waters (Table 4) ranged from 4.4 to 5.4 in the ridgetop profiles (B1S1, B1R)
299 and the deepest slope site B1S2. Sites B1S(3-4) had slightly higher pHs up to 5.7. However, these
300 values may reflect degassing under vacuum in the suction water samplers (White et al., 2005) and

we therefore corrected a selection of these values to determine *in situ* pore water pH by assuming equilibrium between dissolved inorganic carbonate (as alkalinity) and soil gas CO₂ (Table 4, Fig. 3) using PHREEQC (Parkhurst and Appelo, 1999). *In situ* pH (only determined for B1S1 and B1R) ranged from 3.9 to 4.7 at B1S1, generally slightly lower than measured values, and from 4.6 to 5.3 at B1R, generally slightly higher than measured values.

CO₂ partial pressures increased with depth, reaching a maximum of 0.065 atm (6.5%) at 7.3 m depth in B1S1 (the deepest gas sampling point in that profile) and 0.042 atm at 1.5 m depth at B1R, then decreasing to 0.032 atm at 8.2 m depth (Fig. 3). Oxygen partial pressures decreased with depth at both sites, reaching a minimum of 0.127 atm at 7.3 m in B1S1 (Liermann et al., 2015). Site B1S1 exhibited a marked drop in O₂ at 3 m depth, corresponding to a marked increase in CO₂ at the same depth. CO₂ in the soil layers (<1m depth) of the Río Icaos regolith is about double compared to both Bisley sites, but increases only slightly with depth to 0.05 atm at 7.3 m with a corresponding decrease in O₂ to 0.169 atm.

4.3. Mineralogy

Optical microscopy of 9 bedrock thin sections taken from corestones of the volcanoclastic bedrock, obtained by continuous core drilling to 37 m depth (Fig. 1; Buss et al., 2013), reveal tuff breccias with andesitic clasts. Phenocrysts are randomly dispersed in a fine groundmass of volcanic glass that has been largely devitrified to microcrystalline quartz and plagioclase, which in turn has been extensively sericitized, forming fibrous illite, and chloritized. Epidote grains also contribute to the groundmass. Phenocrysts include clinopyroxene (augite), plagioclase and quartz. Orthoclase phenocrysts are present in some thin sections, but not all. Subhedral chlorite grains indicate replacement of biotite or plagioclase and fine, fibrous chlorite grains in coarse clusters make up a large proportion of the groundmass. Magnetite is present as inclusions in augite and plagioclase. Fibrous actinolite pseudomorphs of augite, a hydrothermal alteration product of pyroxenes commonly known as uralite (Deer et al., 2013), surround augite grains and fill cracks.

Quantitative XRD data for 18 drilled bedrock corestone samples is given in Buss et al. (2013), with the average shown in Table 5. In that paper, we identified orthoclase, tourmaline and tentatively identified biotite based on XRD and did not identify amphibole. Subsequent, extensive optical and SEM-EDS analysis of bedrock thin sections has revealed amphibole throughout the rock but no biotite or tourmaline and only very heterogeneously distributed orthoclase (data not shown). The whole-pattern fitting algorithm used to quantify mineral abundance from powder XRD data depends on the standards input to the program (Eberl, 2003) and a tourmaline standard, but not amphibole, was included in analysis of the drilled bedrock. Herein we refer to this phase as

334 amphibole (Table 5). Similarly, we attribute the putative biotite to illite as XRD pattern separation
 335 of these minerals was not definitive but correlation of the quantitative XRD results with bulk
 336 elemental chemistry using HANDLENS (Eberl, 2008) showed that the pattern previously attributed
 337 to biotite is consistent with an Fe-rich illite. Other mineral abundances reported in Buss et al. (2013)
 338 are broadly consistent with thin section observations.

339 Mineralogy of the hand-augered regolith cores is dominated by microcrystalline disordered
 340 kaolinite, microcrystalline quartz, goethite, hematite and some mixed-phase, dioctahedral clays,
 341 consistent with illite (Tables 7-8, Fig. 4). Abundances of hematite and goethite are similar in the
 342 two cores, but the proportions of kaolinite and quartz vary, with B1S1 containing more kaolinite
 343 (>80% at some depths) and less quartz than B1R. Site B1S1 also contains additional minerals in
 344 saprolite and clasts from 9.0-9.3 m depth including chlorite, other clays, orthoclase and plagioclase.
 345 These minerals are not present in any B1R samples. The clasts in the B1S1 core (present at 9.0 and
 346 9.3 m) contain more quartz, chlorite and feldspar, but less hematite, goethite, kaolinite and other
 347 clays than the saprolite matrix at the same depths. Most of the clasts in the B1R core have slightly
 348 less quartz, slightly more kaolinite and similar FeIII-(hydr-)oxide mineral contents than the
 349 surrounding saprolite.

350

351 **5. DISCUSSION**

352 **5.1 Elemental distributions and hydrologic flux**

353 Typical of a coastal watershed, Cl is the dominant anion in the soil pore waters (Table 4). The
 354 variability in pore water Cl reflects precipitation patterns, evapotranspiration (ET), and possible
 355 minor microbial cycling of chlorinated organic compounds (Bastviken et al., 2007). Because Cl
 356 derived from chemical weathering is negligible given the large sea salt inputs and lack of potential
 357 Cl-bearing minerals in the regolith, pore water Cl concentrations can be used to estimate ET and
 358 rates of water movement through the regolith. Assuming 1-D vertical flow, the hydraulic flux, also
 359 known as the fluid flux density, q_h (m yr⁻¹), is equal to the net difference between the annual
 360 precipitation and the ET fluxes, q_{precip} (m yr⁻¹) and q_{ET} (m yr⁻¹), respectively, which in turn is equal
 361 to the product of the precipitation and the ratio of the volume-weighted Cl concentration in
 362 precipitation, $C_{Cl,precip}$ (μM), to that in the pore waters, $C_{Cl,solute}$ (μM) (Table 6; White et al., 2009):

$$363 \quad q_h = q_{precip} - q_{ET} = q_{precip} \left(\frac{C_{Cl,precip}}{C_{Cl,solute}} \right) \quad (2).$$

364 High estimates for ET (~50-60% of rainfall, Eq. 2) in the volcanoclastic and granitic sites are
 365 consistent with estimates of ET in the LCZO determined using other methods (e.g., Schellekens et

al., 2000; Wu et al., 2006; see also compilation in Murphy and Stallard, 2012). The average Cl concentration in the pore waters, $C_{Cl,solute}$, was determined as the average of all depths below 4 m over 2007-2008 and $C_{Cl,precip}$ was determined from the volume-weighted average of monthly openfall samples at site B1R (Table 4). Fluid flux densities were not calculated for slope sites B1S2, B1S3 or B1S4 because 1-D flow may not be a valid assumption at those locations. The resultant fluid flux densities of $q_h = 1.5 \pm 0.3$ and 1.6 ± 0.2 m yr⁻¹ for B1R and B1S1, respectively (Table 6), are the same within error as that reported for the Río Icacos LG1 regolith ($q_h = 1.28$ m yr⁻¹, White et al., 1998). Note that although the units of fluid flux density, q_h , are here length per unit time, this quantity is intrinsic to the regolith medium and actually represents a volume of water (m³) transported across a regolith area (m²) over time (s) (Hillel, 1982).

The infiltration rate I (m yr⁻¹) describes the macroscopic rate of water movement downward through the regolith and is calculated from the fluid flux density divided by the product of the average porosity, Φ (m³ m⁻³), and saturation, Γ (m³ m⁻³):

$$I = \frac{q_h}{\Phi \Gamma} \quad (3).$$

Porosity, determined from bulk densities and specific gravities, is estimated as 0.47 ± 0.02 and 0.60 ± 0.08 for B1R and B1S1, respectively (Table 1). Saturation, determined from water content and porosity, is estimated as 0.62 ± 0.04 and 0.55 ± 0.07 for B1R and B1S1, respectively (Table 6). The calculated infiltration rates for B1R and B1S1, respectively, are 5.3 ± 0.3 and 5.00 ± 0.01 m yr⁻¹. The Río Icacos site LG1 has average porosity and saturation values of 0.52 and 0.77 m³ m⁻³, respectively (White et al., 1998, based on monthly pore water sampling from 1992-1994), similar to those of the Bisley sites.

Average fluid residence times can be calculated by dividing the profile thicknesses by the infiltration rates (Eq. 3, Table 6). Thus faster infiltration rates yield shorter residence times, ~ 2 years in the Luquillo profiles. Therefore, hydrologic fluxes, and by extension, chemical fluxes, can be expected to respond to changing precipitation patterns on an almost annual timescale. This contrasts to other locations such as Santa Cruz, California, where fluid residence times range from 10-24 years, indicating that the hydrologic fluxes are dependent on decadal scale variations in precipitation (White et al., 2009).

White et al. (1998) reported an infiltration rate of 1.07 m yr⁻¹ and a fluid residence time of 7.93 years for the Río Icacos profile. These values were estimated from hydraulic conductivities and the hydraulic gradient, assuming no ET or lateral flow. To eliminate methodological variation from our comparison between the watersheds, here we recalculated infiltration and residence time in the

398 Río Icacos using the Cl concentration ratio (Eq. 2) and the pore water data from White et al. (1998).
 399 We note, however, the assumption of 1-D flow as a potential source of error in estimating q_h from
 400 Cl concentrations (Eq. 2), because surface runoff or subsurface storm flow would decrease q_h
 401 (leading to lower infiltration rates) but have little effect on pore water Cl concentrations.

402 Contrary to our calculations (Table 6), a previous study determined that the volcanoclastic
 403 regolith is less permeable and has lower infiltration rates than the granitic regolith (Simon et al.,
 404 1990) based mainly on a more rapid response of piezometers to large rainfall events in the granitic
 405 areas. Faster infiltration was implicated in the greater susceptibility to landslides of the granitic
 406 regolith relative to the volcanoclastic regolith (Simon et al., 1990). The discrepancy between those
 407 relative infiltration rates and ours may stem from the saturation values used in our calculations
 408 (Table 6), which were measured on cores taken more than 10 years apart (the granitic cores in the
 409 mid 1990's and the volcanoclastic cores in 2006 and 2007), and the timing and size of storms
 410 preceding core collection may not be comparable. However, we note that below 0.5 m, regolith
 411 porosity at the volcanoclastic site B1S1 is higher than at the granitic site.

412 For elements such as Na, which are not significantly incorporated into, or sorbed onto,
 413 secondary minerals and are not major plant nutrients, input to regolith pore waters is expected to be
 414 via precipitation and chemical weathering. Net weathering contributions of such elements to the
 415 pore water, $c_{j,net}$, are calculated as the difference between the measured concentration of an element
 416 j in the pore waters $c_{j,solute}$, and the ET-corrected concentration of j in precipitation (White et al.,
 417 2009). This correction, which accounts for the concentration of elements as water is removed by
 418 ET, is made by multiplying $c_{j,precip}$ by the ratio of pore water Cl to precipitation Cl (Eq. 2):

$$419 \quad c_{j,net} = c_{j,solute} - c_{j,precip} \left(\frac{c_{Cl,solute}}{c_{Cl,precip}} \right) \quad (4).$$

420 Net solute concentrations (Eq. 4) are zero within error for the majority of the soluble cations
 421 at most depths in most of the profiles, including Na, Ca, Sr, K, Mg, and Al. In contrast, net solute Si
 422 is nearly identical to measured solute Si, because the Si concentration in precipitation is 2 orders of
 423 magnitude lower than Si in the pore waters (Table 4). Thus, precipitation is not a significant source
 424 of Si to the pore water (Fig. 2a-c). Net solute Na concentrations are zero or within error of zero at
 425 most depths at most sites, with concentrations >0 mainly below the rooting zone of B1S(2-4) and at
 426 the soil-saprolite transition of B1R. Due to the close proximity of the ocean, the Luquillo
 427 watersheds receive significant inputs of sea salt Na in precipitation (Gioda et al., 2013), thus it is
 428 expected that the majority of Na in pore water is derived from precipitation. The Bisley regolith is
 429 essentially devoid of plagioclase and solid-state concentrations of Na are below or near detection
 430 (Tables 2, 7-8) thus there is no obvious source for weathering-contributed Na in the regolith.

431 Interestingly, the thicker B1R regolith contains measurable solid-state Na at most depths but no
 432 plagioclase or other likely Na-bearing minerals were detected in the XRD patterns of the regolith
 433 (Table 76). Net solute Mg is within error of zero in most of B1S(2-3) but is >0 below the rooting
 434 zone of B1S1, B1S4 and B1R (Fig. 2d, e). Net solute K is >0 at the top and bottom of B1S1 and
 435 throughout B1S4.

436 5.2. Chemical mobility

437 Weathering profiles develop as a combination of open and closed system processes. Open-system
 438 contributions include mass transfer, which is described by the mass transfer coefficient commonly
 439 known as tau, $\tau_{j,i}$ (Eq. 5; Brimhall and Dietrich, 1987; Anderson et al., 2002), where j represents a
 440 mobile element and i represents a relatively immobile element. Closed-system contributions include
 441 residual enrichment, reflecting changes in density (ρ), and strain ($\varepsilon_{i,w}$, Eq. 6), which reflects volume
 442 changes during weathering.

$$443 \tau_{j,i}^* = \left(\frac{C_{j,w}C_{i,p}}{C_{j,p}C_{i,w}} \right) - 1 \quad (5)$$

$$444 \varepsilon_{i,w} = \frac{\rho_p C_{i,p}}{\rho_w C_{i,w}} - 1 \quad (6)$$

445 The tau equation (5) is equivalent to the negative of the chemical depletion factor (CDF) defined by
 446 Riebe et al. (2003) and is a simplification of a longer-form that includes a term for strain:

$$447 \tau_{j,i} = \frac{\rho_w C_{j,w}}{\rho_p C_{j,p}} (\varepsilon_{i,w} + 1) - 1 \quad (7)$$

448 Both versions of tau assess mass transfer of a mobile element, j , relative to the concentration, C , of
 449 an immobile element, i , in the parent rock, p , and the weathered material, w . Following Chadwick et
 450 al. (1990), the relationship between tau and strain can be used to evaluate the immobility of low
 451 solubility elements and to assess the effect of the variability in concentration, $C_{i,p}$, of these elements
 452 in the parent rock. To do this, we use Equation 7 to calculate the mobility (tau) of Ti using Zr as
 453 immobile and the mobility of Zr using Ti as immobile; these are the two elements most commonly
 454 considered to be immobile during weathering (e.g., Chadwick et al., 1990; White et al., 1998). We
 455 then calculate maximum and minimum values for strain (Eq. 6) using the 1σ value for Zr or Ti
 456 concentrations in the parent rock (protolith composition was assumed to be the average of 18 un-
 457 weathered samples obtained from drill cores, Table 2; Buss et al., 2013). In a plot of tau versus
 458 strain ($\tau_{j,i}$ versus ε_i , Fig. 5), if the maximum to minimum range in strain values for any given sample
 459 overlap with the $\pm 1\sigma$ zone that reflects the variability in parent rock composition, we can consider
 460 the element to be immobile in that sample (Chadwick et al., 1990). If instead $\tau_{j,i}$ versus ε_i plots

below (< 0) the $\pm 1\sigma$ zone, element j has been leached or the concentration of j in the parent for that particular sample was lower than the concentration represented by the $\pm 1\sigma$ zone. Similarly, if $\tau_{j,i}$ versus ε_i plots above (> 0) the $\pm 1\sigma$ zone, element j has been added (transported or translocated to the sample location) or the concentration of j in the parent was greater than the concentration represented by the $\pm 1\sigma$ zone. Strain values < 0 indicate volume collapse or gain of element i , while strain > 0 indicates dilation or loss of element i . If element i is completely immobile and weathering is isovolumetric, $\varepsilon_i = 0$.

Concentrations of Ti in the parent rock (volcaniclastic and granitic) for both watersheds (Bisley and Río Icacos) are less variable than Zr, resulting in narrower $\pm 1\sigma$ zones when Ti immobility is assessed (Fig. 5d-f) than when Zr immobility is assessed (Fig. 5a-c). For the Bisley sites assessed (B1R, B1S1, Figs. 5a-b,d-e), few samples overlap the $\pm 1\sigma$ zone for Ti immobility, with most samples showing enrichment in Zr with respect to Ti ($\tau_{Zr,Ti} > 0$) and positive strain (ε_{Ti}), indicating loss of Ti during weathering in Bisley. In contrast, only the shallowest Río Icacos sample does not overlap the $\pm 1\sigma$ zone for Ti immobility; this sample plots as enriched in Zr relative to Ti, reflecting either dust input of Zr or leaching of Ti, and strain is strongly positive, reflecting dilation by strong bioturbation (Fig. 5f), consistent with previous findings (White et al., 1998) and our field observations. Therefore, Ti appears to be sufficiently immobile in the Río Icacos weathering profile, but mobile in Bisley.

Most samples in each Bisley profile overlap the $\pm 1\sigma$ zone for Zr immobility (Figs. 5a-b) indicating that Zr is relatively immobile during weathering of the volcaniclastic rocks. Average strain with respect to Zr, ε_{Zr} , at site B1S1 is near zero, but the range in strain values is > 1 , which likely reflect the variability of Zr in the parent rock and low Zr concentrations. The B1S1 samples that do not overlap the $\pm 1\sigma$ zone come from the upper part of the profile (< 2.5 m depth) and reflect the loss of Ti with respect to Zr and either volume collapse or gain of Zr from dust with Zr/Ti ratio $>$ bedrock, at these depths. In contrast, the two B1R samples that do not overlap the $\pm 1\sigma$ zone are very deep (14.3 and 15.4 m) where density was only estimated. Strain, ε_{Zr} , is more variable in B1R than B1S1, but still within error of zero at most depths (Fig. 6). All Río Icacos samples also overlap the $\pm 1\sigma$ zone for Zr immobility (Fig. 5c) indicating that Zr as well as Ti is conserved during weathering of the quartz diorite as was shown by White et al. (1998).

Volumetric strain calculations indicate near isovolumetric weathering in B1S1, with slight dilation between 4-8 m and slight collapse above 2 m (Fig. 6a). Site B1R has positive strain values for most of the profile, indicating dilation. Weathering in the Río Icacos regolith was shown to be isovolumetric, based on near-zero volumetric strain calculated from a parent rock composition with

494 a Ti content that was subsequently found to be anomalously low and the appearance of a visibly un-
495 altered parent rock fabric in the saprolite (White et al., 1998). Our re-calculation of strain for LG1,
496 based on an average of all available chemical analyses of the Río Blanco quartz diorite (Seiders,
497 1971; Kesler and Sutter, 1979; White et al., 1998; Turner et al., 2003; Buss et al., 2008; Chabaux et
498 al., 2013), indicates dilation throughout the profile (Fig. 6c). Dilation due to bioturbation near the
499 surface is evident in the field, but the deeper saprolite retains the texture of the granitic protolith to
500 the extent that this can be determined visually. Although some expansion of biotite grains during
501 oxidation of Fe(II) (Buss et al., 2008) and subsequent epitaxial growth of kaolinite (Murphy et al.,
502 1998) are known to occur, it is not clear that these mechanisms are sufficient to produce the modest
503 dilation indicated here and further investigation is merited.

504 Mass transfer calculations reveal mass loss of mineral nutrient elements (K, P, Mg, Fig. 7; and
505 Ca, not shown) in all Bisley profiles, except for B1R, where P is enriched at multiple depths
506 throughout the profile (Fig. 7f) and K is enriched at several depths within the top 4 m (Fig. 7a).
507 Similarly, Fe, Ti, Al, and Si are enriched at several depths throughout the B1R profile, but these
508 less-mobile elements are depleted by about $\leq 50\%$ ($\tau_{j,Zr} = -0.5$) in the other profiles (Fig. 8),
509 although some enrichment in Fe is seen from about 5 to 8 m depth in B1S1 (Fig. 8b). These results
510 suggest that depletion-enrichment profiles develop over time in the volcanoclastic regolith such that
511 even relatively immobile elements are mobilized and either leached from, or translocated within,
512 the profiles. The depletion fronts for K, P, and Mg in the volcanoclastic profiles, B1S(1-4), reveal
513 progressive loss of these elements via chemical weathering with decreasing depth in the regolith
514 (Fig. 7c-d, g-i, l-n). However, most of the loss of these elements relative to the parent rock is not
515 directly documented here because it occurs below the deepest samples in each profile, which are
516 about 25-75% depleted relative to the parent rock (with the exception of the deepest B1S4 sample,
517 which shows no loss of K relative to the parent rock, Fig. 7d). As with the granitic rock, which loses
518 significant mass during spheroidal weathering of corestones below the augerable regolith (Buss et
519 al., 2008), the volcanoclastics also undergo significant mass loss before the corestones disaggregate
520 into regolith. Spheroidal weathering is rare in the volcanoclastics, with rock weathering largely
521 occurring within mm's-thick weathering rinds (Buss et al., 2013) in comparison to the
522 approximately 50 cm spheroidal weathering rindlet sequences in the granitic rock (Buss et al.,
523 2008). The high density of fractures in the volcanoclastic rock (Buss et al., 2013), coupled with the
524 sharp weathering fronts across rinds and the lack of weatherable minerals in the volcanoclastic
525 regolith, highlights the primary importance of weathering of rock surfaces relative to weathering in
526 the regolith. Therefore, solute exports from the watershed are expected to be overwhelmingly
527 dominated by rock weathering rather than regolith weathering in the volcanoclastics. Indeed, S and

528 Mg isotope ratios in the Bisley 1 stream during baseflow are consistent with dominant bedrock-
529 sources of these elements (Chapela Lara et al., 2014; Yi-Balan et al., 2014). Similarly, Ge/Si ratios
530 in the Río Icacos during baseflow reflect weathering reactions that only occur in the spheroidally
531 weathering bedrock (Kurtz et al., 2011).

532 Near-zero net solute concentrations for most soluble cations throughout most of the
533 volcanoclastic regolith profiles demonstrate that contemporary chemical weathering of minerals in
534 the regolith does not, generally, produce significant solutes. The notable exception is Si, which has
535 high net concentrations in the pore water throughout all of the profiles, reflecting contemporary
536 release of Si during weathering (Fig. 2). Net concentrations of Mg and K at the bottom of some of
537 the profiles likely reflect contemporary weathering of primary minerals near the rock-regolith
538 interfaces.

539 **5.3. Mineral weathering reactions**

540 *5.3.1. Mineral weathering fronts*

541 A *weathering front* is the zone over which a weathering reaction (e.g., plagioclase dissolution)
542 occurs; in a 1-D profile (e.g., a ridgetop), it extends from the depth at which the reaction begins to
543 the depth at which the reaction is complete or, in the case of an incompletely developed weathering
544 profile, to the land surface. When a tau or net solute profile can be associated with a specific
545 mineral weathering reaction, it describes the weathering front of that reaction over the timescale of
546 regolith development or the timescale of water infiltration, respectively (White, 2002). We identify
547 weathering fronts in the Bisley and Río Icacos depth profiles (solid-state and solute) based on linear
548 regressions (Figs. 2, 7-8; Table 9). Where more than one front may be identified in a depth profile,
549 we opt for the most inclusive front (extending over a greater regolith thickness), providing a greater
550 number of data points. An exception is where elemental fronts can be directly attributed to an
551 individual mineral as identified in quantitative XRD depth profiles (Fig. 4h, Tables 7-8). We focus
552 only on the ridgetop profiles B1R, B1S1 and LG1 when discussing solute weathering fronts because
553 possible lateral solute transport cannot reasonably be ignored in the slope profiles (B1S2-4).

554 Weathering fronts for primary minerals (with the exception of some illite) in the solid Bisley
555 regolith profiles (excluding the few weathered clasts) are located only at the corestone-regolith
556 interfaces at the bottom of sites B1S(1-4). The XRD data (Table 8), shows that the Bisley regolith is
557 devoid of primary minerals other than quartz and illite except at the bottom of B1S1 (XRD analysis
558 was only done on B1R and B1S1 samples). No weathering fronts were identified in the B1R solid
559 profiles and those tau plots likely reflect significant chemical redistribution. Near-total depletion of
560 Na and Ca in all profiles indicates that the weathering fronts for the minerals containing these

561 elements (i.e., plagioclase, pyroxene, amphibole, epidote, prehnite) occur below the depth of
562 augering. In the disturbed site, B1S3 (sited on a tree throw), no weathering fronts were detected and
563 this site was not used for further investigation or calculations. At sites B1S1, B1S2, B1S4 and LG1
564 tau profiles for Mg indicate mineral weathering fronts over, approximately, the deepest 1-2 meters
565 of the profiles (Fig. 7). As these tau profiles do not reach parent composition at depth, the fronts
566 likely begin within the weathering rinds, which were not retrievable by hand-augering. Similarly,
567 sites B1S1 and LG1 show P weathering fronts at the bottom of the profiles Figs. 7g and 7j). In
568 contrast, K weathering fronts are evident in sites B1S1, B1S4 and LG1 that span most of the
569 regolith thickness (Figs. 7b and 7d-e). Site B1S1 also has a slight, but significant, Mg front that
570 spans about 8 m of regolith (Fig. 7l).

571 Based on the mineralogical composition of the weathering rinds (Buss et al., 2013), it is likely
572 that Mg is largely lost from chlorite, pyroxene and amphibole and K is lost mainly from illite during
573 rind formation. The absence of pyroxene and amphibole in the regolith means we can attribute the
574 Mg front here to chlorite dissolution, where chlorite is detected (>9 m depth, Fig. 4). Above 9 m
575 depth, the source of Mg is less obvious. Illite dissolution could release both Mg and K, but net
576 solute profiles for these elements appear unrelated (e.g., $R^2 = 0.00$ in B1S1). However, net solute
577 Mg and Si concentrations both correlate to NH_4 -acetate extractable Mg at site B1R (there are
578 insufficient matching depths to determine this for B1S1), both with R^2 of 0.78, consistent with
579 dissolution of a silicate phase containing exchangeable Mg (Fig. 9). Indeed, in the B1S1 regolith,
580 about 61 mol% of total extractable cations are Mg (44% in B1R), although these could be present in
581 the regolith sorbed to oxides or organics as well as to silicates. In contrast, extractable K and net
582 solute Si do not correlate ($R^2 = 0.02$) and net solute K is below detection at all but the two
583 shallowest depths. Illite is also the only K-containing mineral phase identified by XRD in the
584 regolith profile above 9 m depth (Table 8). Therefore, although illite dissolves in the upper portion
585 of the B1S1 regolith (above 7.6 m) as evident in the depletion profile calculated from mineral
586 abundance (Fig. 10), the small amount of K this dissolution releases to pore water is insignificant.
587 Below these depths, the tau values for illite and kaolinite form addition profiles, reflecting clay
588 formation (Fig. 10). Interestingly, this clay formation coincides with a solid-state depletion profile
589 in K below about 8 m depth in B1S1 (Fig. 7b), which is consistent with loss of K ions during
590 oxidation of Fe(II) in the clays to maintain charge balance, and/or removal of K as dioctahedral
591 clays weather into simpler phases (e.g., kaolinite). The volcanoclastic bedrock contains only minor
592 apatite (<0.5 vol%), which is unlikely to survive the intensive weathering at the rock-regolith
593 interface. Thus we tentatively attribute the B1S1 P tau profile (Fig. 7g) to the release of sorbed or
594 organic P of atmospheric origin, although further investigation is needed.

Solute weathering fronts are determined from net solute concentrations (Fig. 2), which are measured pore water concentrations corrected for rainfall inputs and ET (Eq. 4). A decrease in a net solute with decreasing depth reflects progressive release of that solute from the solid phase, generally attributed to dissolution (e.g., White, 2002). Solute weathering fronts for Mg and Si are apparent in the three ridgetop regolith profiles: B1R, B1S1 and LG1 below the rooting depth (Fig. 2). In site B1S1, we attribute the Mg front to chlorite dissolution below 9 m depth, where chlorite was identified by XRD (Table 8, Fig. 4h). The B1S1 Mg front above this depth may represent dissolution of some combination of trace residual chlorite, illite and impure kaolinite and/or the release of sorbed Mg.

Above ~1 m depth at these sites, net solute Mg increases, which we attribute to throughfall and decomposition inputs of Mg not accounted for in Equation 4. Over the timescale of regolith formation, these inputs represent internal fluxes expected to be at steady state, which may not hold true on the timescale of water infiltration. As the chemistry of throughfall varies significantly in space and time here (Heartsill-Scalley et al., 2007), we will only use fronts identified below rooting depth to calculate rates (Section 5.3.2).

Net Si solute concentrations below 2 m depth in the three ridgetop sites indicate dissolution of silicate minerals (Fig. 2). Above this depth in B1S1 and B1R, net Si increases towards the surface, which may reflect more rapid weathering (i.e., Si release by weathering is not in steady state over the thickness of the profile) and/or an additional source of non-rainfall Si such as the dissolution of phytoliths, as was identified in the upper 30 cm of ridgetop soils in the LG1 profile based on Si isotopes (Ziegler et al., 2005) and Ge/Si ratios (Lugolobi et al., 2010). Dissolution of both biotite and quartz have been documented in the LG1 regolith (Murphy et al., 1998; Schulz and White, 1999).

5.3.2. Long-term weathering rates and fluxes

Solid-state weathering fronts reflect cumulative weathering over the timescale of regolith development. Using a 1-D, linear approximation, we estimate long-term, average mineral reaction rates, R_{LT} ($\text{mol m}^{-2} \text{s}^{-1}$), normalized to mineral surface area, from the gradients of these fronts (White, 2002):

$$R_{LT} = 10^{-3} \frac{\omega}{\varphi \beta s b_s} \quad (8)$$

where φ (g g^{-1}) is the mass fraction of the mineral in the weathering material, β (mol mol^{-1}) is the stoichiometric coefficient of the element in the mineral, s ($\text{m}^2 \text{g}^{-1}$) is the specific surface area of the mineral, b_s (m kg mol^{-1}) is the weathering gradient, and ω (m s^{-1}) is the weathering advance rate.

627 The weathering advance rate reflects the lowering of the rock-regolith interface, for which we use
 628 the average regolith production rate, $334 \pm 46 \text{ mm ky}^{-1}$, calculated for the Bisley watershed from the
 629 U-series regolith age (Dosseto et al., 2012). We estimate a reactive surface area, s , for illite and
 630 chlorite using the relationship between the spherical geometric surface area and BET surface area
 631 (Helgeson et al., 1984; White and Brantley, 2003):

$$632 \quad s = \frac{6\lambda}{\rho D} \quad (9)$$

633 with a surface roughness factor, λ , of 110 for un-weathered micas, which also accounts for the non-
 634 spherical geometry of layered silicate minerals (White and Brantley, 2003). Mineral densities, ρ , of
 635 2.65 and 2.75 g cm^{-3} for chlorite and illite, respectively, and the average groundmass grain size
 636 diameter, D , of $14 \text{ }\mu\text{m}$ (determined from SEM images), yielded specific surface areas of 18 and 17
 637 $\text{m}^2 \text{ g}^{-1}$ for chlorite and illite, respectively. Kaolinite surface area was estimated at $35 \text{ m}^2 \text{ g}^{-1}$, which is
 638 typical for soil kaolinites (Singh and Gilkes, 1992). The stoichiometric coefficient, β , is 4.6 mol Mg
 639 mol^{-1} chlorite, based on electron microprobe analysis of bedrock thin sections. The kaolinite and
 640 illite dissolution rates are calculated using the quantitative XRD abundances rather than interpreted
 641 from elemental profiles, therefore β is not included in the calculation for kaolinite or illite. The mass
 642 fractions of the minerals in the weathering bedrock, ϕ , are 0.23 g g^{-1} chlorite, 0.009 g g^{-1} illite and
 643 0.004 g g^{-1} kaolinite (Buss et al., 2013). Finally, the weathering gradients (Table 9) are $6 \pm 1 \text{ m kg}$
 644 $\text{mol}^{-1} \text{ Mg}$ for chlorite (over $8.2\text{-}9.3 \text{ m}$ depth, $R^2 = 0.69$), $30 \pm 10 \text{ m kg mol}^{-1}$ illite (over $0\text{-}7.6 \text{ m}$
 645 depth, $R^2 = 0.95$) and $7.5 \pm 0.6 \text{ m kg mol}^{-1}$ kaolinite (over $0\text{-}4.9 \text{ m}$ depth, $R^2 = 0.76$). The resulting
 646 long-term mineral weathering rates are: $8.9 \times 10^{-14} \text{ mol chlorite m}^{-2} \text{ s}^{-1}$, $2.1 \times 10^{-14} \text{ mol illite m}^{-2} \text{ s}^{-1}$
 647 and $4.0 \times 10^{-14} \text{ mol kaolinite m}^{-2} \text{ s}^{-1}$ (Table 10). This kaolinite dissolution rate ($\log R = -13.5$ to -
 648 13.3 , with uncertainty) is within range of laboratory rates ($\log R = -14.1$ to -12.4) for experiments
 649 conducted at ambient temperatures within the pH range of the B1S1 pore waters in the kaolinite
 650 dissolution zone (pH 4-5), but with lower specific surface areas ($7.5\text{-}18 \text{ m}^2 \text{ g}^{-1}$) than assumed here
 651 ($35 \text{ m}^2 \text{ g}^{-1}$), as compiled by Bandstra et al. (2008). The chlorite dissolution rate at the bottom of the
 652 saprolite in Bisley ($\log R = -13.2$ to -13.0) is nearly as fast as laboratory rates at pH 4-5 and ambient
 653 temperatures ($\log R \sim -13$ to -11) as compiled by Alekseyev (2007) and faster than field rates: $\log R$
 654 $= -17$ to -16.3 in shale at the Susquehanna/Shale Hills CZO (SSHCZO) in Pennsylvania, USA (Jin
 655 et al., 2010) and $\log R = -13.9$ to -15.8 in Amazonian ultramafic schists (Freyssinet and Farah,
 656 2000). There are fewer published rates available for illite dissolution, but the Bisley illite
 657 dissolution rate ($\log R = -13.5$ to -13.9) is also consistent with laboratory rates ($\log R = -14$ to -
 658 13.7) measured at pH 3.0-4.7 and 25°C (Köhler et al., 2003; Allan et al., 2011; Bibi et al., 2011)

659 and orders of magnitude faster than field rates ($\log R = -16.7$ to -16) for the SSHCZO shale (Jin et
660 al., 2010).

661 Not all gradients can be easily, or solely, attributed to a specific mineral. In this case we can
662 use them to calculate long-term elemental fluxes per unit area of weathering regolith, Q_{LT} (mol m^{-2}
663 s^{-1}):

$$664 \quad Q_{LT} = 10^{-3} \frac{\omega \rho_p \Delta z}{b_s} \quad (10)$$

665 where Δz is the depth (m) over which the gradient b_s is calculated; that is, the mass of the element is
666 only integrated over the vertical distance in which the element increases with depth in the augered
667 regolith. Here we calculate the long-term elemental fluxes through the volcanoclastic B1S1, B1S2,
668 and B1S4 regolith profiles and the granitic LG1 regolith profile, the latter using regolith data from
669 Buss (2006) (Table 2). Note that these fluxes (and the mineral weathering rates calculated above)
670 only reflect weathering within the augered regolith as our profiles do not extend into the non-
671 augerable bedrock, where substantial weathering occurs along fractures (Buss et al., 2013). As
672 noted previously, profile B1R does not contain any clear solid-state weathering fronts (Figs. 7-8).
673 The resultant long-term Si fluxes (Table 10) are identical within uncertainty for the three other
674 Bisley sites (a Si gradient was not apparent in the Río Icacos profile, consistent with retention of Si
675 in secondary phases and with previous studies, White et al., 1998; White, 2002). Solid-state fluxes
676 of Mg, K and P are several orders of magnitude lower in Río Icacos than in Bisley (Table 10),
677 despite similar abundances of P and higher Mg and K abundance in the Río Icacos regolith.

678 5.3.3. Contemporary weathering

679 Absolute mass change with depth per unit volume is significantly greater in solid profiles than in
680 solute profiles, because while solid-state gradients reflect cumulative weathering over the age of
681 regolith, typically $\sim 10^4$ - 10^6 years, solute gradients reflect contemporary weathering, typically over
682 ~ 1 -100 years, the timescale of water infiltration into regolith. The rates of these reactions can be
683 compared to determine whether or not a reaction is in steady-state. Similar to the long-term fluxes
684 calculated above, short-term weathering solute fluxes, Q_{ST} ($\text{mol m}^{-2} \text{s}^{-1}$), can be calculated from the
685 net solute gradients and the fluid flux density, q_h (m s^{-1}) (White, 2002):

$$686 \quad Q_{ST} = 10^3 \frac{q_h \Gamma \Delta z}{b_f} \quad (11)$$

687 where b_f is the weathering gradient in the fluid phase (m L mol^{-1}), Γ is the saturation ($\text{m}^3 \text{m}^{-3}$), Δz is
688 the depth (m) over which the gradient is measured and 10^3 is a unit conversion factor (Tables 6 and
689 9).

690 Solute gradients in the volcanoclastic watershed were only determined for the ridgetop sites
691 B1R and B1S1 (Table 9). The resulting fluxes (Table 10) represent only solute production occurring
692 within the regolith profiles, not catchment fluxes, which may include weathering products from
693 other parts of the critical zone. The regolith Mg and Si solute fluxes (Eq. 11) in B1R and B1S1 are
694 about an order of magnitude lower than the Si fluxes (Table 10). The solute flux in the granitic
695 ridgetop (LG1) regolith was calculated from weathering gradients previously measured (Tables 9-
696 10; Schulz and White, 1999; White, 2002) and q_h and Γ values calculated here (Table 6). The Mg
697 and K solute fluxes in the granitic regolith are faster than those in the volcanoclastic regolith (K was
698 below detection in most volcanoclastic pore waters; Table 10), reflecting biotite dissolution in the
699 granitic regolith (Murphy et al., 1998) - and mostly secondary mineral dissolution in the
700 volcanoclastic regolith. Although contemporary weathering fluxes in the volcanoclastic Bisley
701 *regolith* are apparently slow (Table 10), contemporary *whole-watershed* weathering fluxes are
702 likely faster due to the rapid weathering of primary minerals in fractured bedrock below the
703 augerable regolith (Buss et al., 2013). Indeed, solute weathering fluxes of Mg, K and Si averaged
704 over 1991-2005 (Stallard, 2012) were faster in the river that drains the Bisley catchments (Río
705 Mameyes) than in the Bisley regolith and nearly identical to those in the Río Icacos (Table 10).

706 The long-term fluxes calculated from solid-state profiles are several orders of magnitude
707 larger than the contemporary fluxes calculated from solute profiles in the volcanoclastic regolith,
708 consistent with faster *regolith* weathering in the past (Table 10). In contrast, the granitic regolith of
709 site LG1 has similar long-term and contemporary weathering fluxes. The granitic watershed has
710 slower ridgetop weathering advance rates than the volcanoclastic watershed ($\sim 50 \text{ m Ma}^{-1}$ versus
711 $\sim 330 \text{ m Ma}^{-1}$, respectively; Brown et al., 1995; Dosseto et al., 2012). Therefore, a 10 m granitic
712 regolith is older than a 10 m volcanoclastic regolith in this CZO, yet the older granitic regolith
713 retains more primary minerals, namely biotite, which produces the faster contemporary Mg and K
714 weathering fluxes as compared to the volcanoclastic regolith. In contrast, the primary minerals in the
715 volcanoclastic regolith dissolve almost completely at the rock-regolith interface (Tables 5, 7-8; Buss
716 et al., 2013).

717 **5.4. Importance of lithology to weathering profiles and rates**

718 Lithology is arguably the primary difference between the two catchments discussed here (Bisley
719 and Río Icacos); these two rock types (andesitic meta-volcanoclastic and tonalite) differ in

720 mineralogy, grain size and porosity. Other differences between the catchments, of potential
721 importance to weathering, are mean annual precipitation (slightly higher in Río Icacos) and bedrock
722 age (much older in Bisley). Weathering of the bedrock has produced thick regolith profiles on both
723 rock types. The augerable, ridgetop regolith in Bisley is thicker than in Río Icacos: 9-16 m and 5-9
724 m, respectively, as evidenced by observations of high-elevation landslides in both watersheds and
725 by augering to refusal at 8 ridgetop locations in Bisley for this study and roughly 30 times by us and
726 other groups in the Río Icacos (e.g., White et al., 1998; Schellekens et al., 2004; Buss et al., 2005).
727 The thicker regolith on the relatively stable Bisley ridgetops likely reflects the faster regolith
728 production rate ($334 \pm 46 \text{ mm ky}^{-1}$) relative to Río Icacos ($45 \pm 12 \text{ mm ky}^{-1}$), as estimated from U-
729 series analysis of these regolith and weathering rock (saprock) profiles (Dosseto et al., 2012;
730 Chabaux et al., 2013). The U-series rates for Río Icacos corroborate earlier denudation rates
731 estimated from elemental and isotopic mass balances in water (stream or pore water) and saprolite
732 profiles (McDowell and Asbury, 1994; White et al., 1998; Turner et al., 2003; Pett-Ridge et al.,
733 2009), and cosmogenic ^{10}Be nuclides in stream sediments (Brown et al., 1995; Riebe et al., 2003).
734 The regolith production rates indicate that the Bisley regolith is younger than the Río Icacos
735 regolith (40-60 ky at site B1R versus 100-200 ky in Río Icacos; Dosseto et al., 2012; Chabaux et al.,
736 2013) despite the higher erosion rate in the Río Icacos compared to the Bisley watershed (0.58 and
737 0.40 mm y^{-1} , respectively; Larsen, 2012) and despite the older age of the volcanoclastic Bisley
738 bedrock compared to the granitic intrusion of the Río Icacos (~100 Ma versus 47 Ma, respectively;
739 Jolly et al., 1998; Smith et al., 1998).

740 Regolith production rates are contingent upon weathering reactions at the bedrock-regolith
741 interface and work is ongoing to identify and quantify the earliest reactions in the Bisley bedrock.
742 Incipient chemical weathering reactions may be either dissolution or oxidation reactions and as such
743 are dependent on the supply of acid (primarily CO_2) or O_2 , respectively (Brantley et al., 2014).
744 Consequently, processes that affect the gradients of these gases in regolith may thereby influence
745 the weathering fronts that control regolith formation, even if these fronts are located in bedrock.
746 Regolith gradients in O_2 and CO_2 often mirror one another due to heterotrophic microbial
747 respiration, which consumes O_2 and produces CO_2 ; as a result, regolith microorganisms may either
748 enhance or retard the bedrock weathering rate, depending on whether the weathering front is
749 controlled by dissolution or oxidation reactions, respectively. Of the three LCZO sites where gas
750 profiles were measured (B1S1, B1R and LG1), only B1S1 contains an “elbow”, or bend, in the gas
751 profiles, characteristic of strong biotic influence (Fig. 3; Brantley et al., 2014). The elbow at ~2 m
752 depth coincides with a change in the makeup of the microbial community and a drop in
753 heterotrophic cell numbers that persists to the bottom of the augered regolith (Liermann et al.,
754 2015). Total microbial cell numbers in the Río Icacos profile, LG1, are roughly an order of

755 magnitude larger than in B1S1 throughout the profile, with large changes at about 1 and 4 m depth
756 (Buss et al., 2005). Although the limited pore gas data presented here does not capture the full
757 temporal variability, the relatively high O₂ content throughout LG1 (and B1R) suggests that
758 microbial reduction of O₂ may be less significant than abiotic processes over the measured depths
759 than in the B1S1 profile. Alternatively, microbial elbows in gas concentrations may occur deeper
760 than the sampled depths.

761 Brantley et al. (2014) proposed that dissolution versus oxidation control of weathering fronts
762 may be contingent upon the amount of FeO in the bedrock, such that Fe(II)-oxidation reactions use
763 up O₂ quickly in Fe(II)-rich rock, allowing the CO₂-driven dissolution front to extend deeper,
764 whereas O₂ is able to penetrate deeper in Fe(II)-poor lithologies. The initiation of chemical
765 weathering by Fe(II)-oxidation has been identified in the Río Icacos tonalite (Buss et al., 2008), in
766 high-grade metamorphic charnokite in Sri Lanka (Behrens et al., 2015), granite in the Virginia
767 Piedmont, USA (Bazilevskaya et al., 2013) and shale in Pennsylvania, USA (Brantley et al., 2013).
768 The Bisley andesitic volcanoclastic rock has significantly more FeO (6.1 wt%) compared to the
769 granitic rock in the Río Icacos catchment (2.7%, Fletcher et al., 2006; Buss et al., 2008). In the Río
770 Icacos catchment, regolith formation is initiated by reaction-driven fracturing of the bedrock, in
771 which O₂ diffuses into the rock and oxidizes Fe(II) in biotite, which leads to a build-up of elastic
772 strain energy, ultimately causing a spheroidal fracture (Fletcher et al., 2006; Buss et al., 2008).
773 Evidence for spheroidal weathering is rare in Bisley rocks and biotite is not present. However,
774 unlike the granitic bedrock, the volcanoclastic bedrock may not require physical fracturing to initiate
775 dissolution of primary minerals as porosity in the un-weathered bedrock is significantly greater: $8 \pm$
776 4% in the volcanoclastic versus $1 \pm 1\%$ for the granitic rock (Buss et al., 2013; Navarre-Sitchler et
777 al., 2013). The volcanoclastic rocks also contain veins and bedding planes that may provide reactive
778 fluids with additional access to weatherable minerals. In addition, the minerals in the volcanoclastic
779 bedrock have higher surface area owing to smaller grain size and a higher proportion of weatherable
780 minerals (i.e., non-quartz silicates). These lithological characteristics contribute to a faster chemical
781 weathering at the volcanoclastic rock-regolith interfaces (Buss et al., 2013) than at the granitic
782 interfaces. These interfaces represent weathering hotspots such that weathering export to the rivers
783 is likely dominated by fluxes from the fractured bedrock in the deep critical zone (e.g., Kurtz et al.,
784 2011; Chapela Lara et al., 2014) and thus contemporary *regolith* weathering fluxes may only be of
785 significance to the local ecosystem.

786

787 6. CONCLUSIONS

788 We compared solid and solute weathering profile data from an andesitic, meta-volcaniclastic
789 catchment (Bisley) to a nearby granitic (tonalite) catchment (Río Icacos) to assess the influence of
790 lithology on weathering mechanisms and rates, and on mineral nutrient availability. We determined
791 that Ti is not conserved in the volcaniclastic profiles, but that Zr is effectively immobile, except
792 near the surface where dust likely contributes additional Zr. Similarly, Zr is effectively immobile in
793 the granitic regolith although Ti is also immobile at all but the shallowest depth. Volumetric strain
794 was recalculated and found to be positive in the granitic profile (LG1), indicating dilation, but
795 nearly zero at most depths in the volcaniclastic profiles, indicating largely isovolumetric
796 weathering.

797 Solid-state weathering fronts for primary minerals in the volcaniclastic regolith exist only
798 near the corestone-regolith interfaces at the bottom of the augered profiles, although weathering
799 fronts for dissolving clay minerals are evident at shallower depths. Solute weathering fronts in the
800 volcaniclastic profiles, determined from pore water concentrations corrected for rainfall and ET,
801 were only detected for Si and Mg. The solute Mg front is attributed to chlorite dissolution below 9
802 m depth and to dissolution of residual phases or release of sorbed Mg above this depth.

803 Long-term K and P fluxes are several orders of magnitude higher in the volcaniclastic regolith
804 than in the granitic regolith, despite solid-state concentrations of P that are nearly the same and of K
805 that are greater in the granitic regolith. Contemporary (net solute) Mg and Si fluxes are similar in
806 the two lithologies, despite arising from different mineral weathering reactions. This similarity does
807 not carry over to the riverine solute concentrations, which vary with lithology and are likely fed by
808 weathering reactions occurring along bedrock fractures, deeper in the critical zone. The long-term
809 (~40 kyrs) elemental fluxes are larger than the contemporary (~2 yrs) fluxes in the volcaniclastic
810 catchment, indicating faster weathering in the regolith in the past. Despite the thicker, more
811 depleted regolith, long-term fluxes of Mg, Si, K and P are also larger in the andesitic volcaniclastic
812 Bisley regolith than in the granitic Río Icacos regolith, highlighting the primary control of lithology
813 on weathering fluxes.

814

815 **ACKNOWLEDGMENTS**

816 This article is dedicated to the memory of our friend and analytical chemist Davisson Vivit (USGS).
817 We also thank USGS personnel for field and laboratory support: Manuel Rosario-Torres, James
818 Shanley, Alex Blum, Bill Evans and Mark Huebner as well as Festo Lugolobi (Boston Univ.), Joel
819 Moore (Towson Univ.) and Carlos Estrada (USFS) and University of Bristol students Bethany
820 Rathbone, Jessica Ecott, and Anne Hunt for optical petrography. We also acknowledge the
821 invaluable advice of Fred Scatena (in memoriam) and funding support from the USGS Water

822 Energy and Biogeochemical Budgets Project of the National Research Program, the NSF Luquillo
823 CZO (NSF EAR-0722476), and PhD fellowships from NERC (for O.W. Moore) and Conacyt (for
824 M. Chapela Lara). We also thank Associate Editor Christophe Tournassat for helpful review and
825 editorial comments as well as those of 3 anonymous reviewers.

826 REFERENCES

- 827 Alekseyev, V.A. (2007) Equations for the dissolution reaction rates of montmorillonite, illite, and chlorite.
828 *Geochemistry International* 45, 770-780.
- 829 Allan, M.M., Turner, A. and Yardley, B.W.D. (2011) Relation between the dissolution rates of single
830 minerals and reservoir rocks in acidified pore waters. *Appl. Geochem.* 26, 1289-1301.
- 831 Anderson, S.P., Dietrich, W.E. and Brimhall, G.H. (2002) Weathering profiles, mass-balance analysis, and
832 rates of solute loss: Linkages between weathering and erosion in a small, steep catchment.
833 *Geological Society of America Bulletin* 114, 1143-1158.
- 834 Bandstra, J.Z., Buss, H.L., Campen, R.K., Liermann, L.J., Moore, J., Hausrath, E.M., Navarre-Sitchler, A.K.,
835 Jang, J.-H. and Brantley, S.L. (2008) Appendix: Compilation of Mineral Dissolution Rates, in:
836 Brantley, S.L., Kubicki, J.D., White, A.F. (Eds.), *Kinetics of Water-Rock Interaction*. Springer, New
837 York, pp. 737-823.
- 838 Bastviken, D., Thomsen, F., Svensson, T., Karlsson, S., Sanden, P., Shaw, G., Matucha, M. and Oberg, G.
839 (2007) Chloride retention in forest soil by microbial uptake and by natural chlorination of organic
840 matter. *Geochim. Cosmochim. Acta* 71, 3182-3192.
- 841 Bazilevskaya, E., Lebedeva, M., Pavich, M., Rother, G., Parkinson, D.Y., Cole, D. and Brantley, S.L. (2013)
842 Where fast weathering creates thin regolith and slow weathering creates thick regolith. *Earth Surface*
843 *Processes and Landforms* 38, 847–858.
- 844 Bazilevskaya, E., Lebedeva, M., Pavich, M., Rother, G., Parkinson, D.Y., Cole, D. and Brantley, S.L.
845 (2013) Where fast weathering creates thin regolith and slow weathering creates thick regolith. *Earth*
846 *Surface Processes and Landforms* 38, 847-858.
- 847 Behrens, R., Bouchez, J., Schuessler, J.A., Dultz, S., Hewawasam, T. and Von Blanckenburg, F. (2015)
848 Mineralogical transformations set slow weathering rates in low-porosity metamorphic bedrock on
849 mountain slopes in a tropical climate. *Chem. Geol.* 411, 283-298.
- 850 Berner, R.A. (2008) Addendum to “Inclusion of the Weathering of Volcanic Rocks in the GEOCARBSULF
851 Model” (R. A. Berner, 2006, V. 306, p. 295–302). *Amer. J. Sci.* 308, 100-103.
- 852 Berner, R.A. and Berner, E.K. (1997) Silicate weathering and climate, in: Ruddiman, W.F. (Ed.), *Tectonic*
853 *Uplift and Climate Change*. Plenum Press, New York, pp. 353-364.
- 854 Bibi, I., Singh, B. and Silvester, E. (2011) Dissolution of illite in saline–acidic solutions at 25°C. *Geochim.*
855 *Cosmochim. Acta* 75, 3237-3249.
- 856 Bluth, G.S. and Kump, L.R. (1994) Lithologic and climatic controls of river chemistry. *Geochimica*
857 *Cosmochimica Acta* 58, 2341-2359.

858 Brantley, S.L., Holleran, M.E., Jin, L. and Bazilevskaya, E. (2013) Probing deep weathering in the Shale
859 Hills Critical Zone Observatory, Pennsylvania (USA): the hypothesis of nested chemical reaction
860 fronts in the subsurface. *Earth Surface Processes and Landforms* 38, 1280-1298.

861 Brantley, S.L., Lebedeva, M. and Bazilevskaya, E. (2014) 6.15 - Relating Weathering Fronts for Acid
862 Neutralization and Oxidation to pCO₂ and pO₂, in: Turekian, H.D.H.K. (Ed.), *Treatise on*
863 *Geochemistry* (Second Edition). Elsevier, Oxford, pp. 327-352.

864 Brantley, S.L. and White, A.F. (2009) Approaches to modeling regolith, in: Oelkers, E.H., Schott, J. (Eds.),
865 *Thermodynamics and Kinetics of Water-Rock Interaction*. Mineralogical Society of America,
866 Washington, D.C., pp. 435-484.

867 Brimhall, G. and Dietrich, W.E. (1987) Constitutive mass balance relations between chemical composition,
868 volume, density, porosity, and strain in metasomatic hydrochemical systems: results on weathering
869 and pedogenesis. *Geochim. Cosmochim. Acta* 51, 567-587.

870 Brown, E.T., Stallard, R., Larsen, M.C., Raisbeck, G.M. and Yiou, F. (1995) Denudation rates determined
871 from the accumulation of in situ-produced ¹⁰Be in the Luquillo Experimental Forest, Puerto Rico.
872 *Earth and Planetary Science Letters* 129, 193-202.

873 Buss, H.L. (2006) *Biogeochemical Weathering of Iron-Silicate Minerals*, Geosciences. The Pennsylvania
874 State University, University Park, PA, p. 203.

875 Buss, H.L., Brantley, S.L., Scatena, F.N., Bazilevskaya, E.A., Blum, A., Schulz, M., Jimenez, R., White,
876 A.F., Rother, G. and Cole, D. (2013) Probing the deep critical zone beneath the Luquillo
877 Experimental Forest, Puerto Rico. *Earth Surface Processes and Landforms* 38, 1170-1186.

878 Buss, H.L., Bruns, M.A., Schultz, M.J., Moore, J., Mathur, C.F. and Brantley, S.L. (2005) The coupling of
879 biological iron cycling and mineral weathering during saprolite formation, Luquillo Mountains,
880 Puerto Rico. *Geobiology* 3, 247-260.

881 Buss, H.L., Mathur, R., White, A.F. and Brantley, S.L. (2010) Phosphorus and iron cycling in deep saprolite,
882 Luquillo Mountains, Puerto Rico. *Chem. Geol.* 269, 52-61.

883 Buss, H.L., Sak, P.B., Webb, S.M. and Brantley, S.L. (2008) Weathering of the Rio Blanco quartz diorite,
884 Luquillo Mountains, Puerto Rico: Coupling oxidation, dissolution, and fracturing. *Geochim.*
885 *Cosmoch. Acta* 72, 4488-4507.

886 Chabaux, F., Blaes, E., Stille, P., di Chiara, R.R., Dosseto, A., Pelt, E., Ma, L., Buss, H.L. and Brantley, S.L.
887 (2013) Regolith formation rate from U-series nuclides: Implications from the study of a spheroidal
888 weathering profile in the Rio Icacos watershed (Puerto Rico). *Geochim. Cosmochim. Acta* 100, 73-
889 95.

890 Chadwick, O.A., Brimhall, G.H. and Hendricks, D.M. (1990) From black box to a grey box: a mass balance
891 interpretation of pedogenesis. *Geomorphology* 3, 369-390.

892 Chapela Lara, M., Buss, H.L., Pogge von Strandmann, P.A.E., Dessert, C. and Gaillardet, J. (2014) Controls
893 on the mg cycle in the tropics: insights from a case study at the Luquillo Critical Zone Observatory.
894 *Procedia Earth and Planetary Science* 10, 200-203.

895 Deer, W.A., Howie, R.A. and Zussman, J. (2013) An Introduction to the Rock-Forming Minerals, 3 ed. The
896 Mineralogical Society, London.

897 Dessert, C., Dupre, B., Francois, L., Schott, J., Gaillard, J., Chakrapani, G. and Bajpai, S. (2001) Erosion of
898 Deccan Traps determined by river geochemistry: impact on global climate and the $^{87}\text{Sr}/^{86}\text{Sr}$ ratio of
899 seawater. *Earth Planet. Sci. Lett.* 188, 459-474.

900 Dessert, C., Dupre, B., Gaillardet, J., Francois, L.M. and Allegre, C.J. (2003) Basalt weathering laws and the
901 impact of basalt weathering on the global carbon cycle. *Chem. Geol.* 202, 257-273.

902 Dosseto, A., Buss, H.L. and Suresh, P.O. (2012) Rapid regolith formation over volcanic bedrock and
903 implications for landscape evolution. *Earth and Planetary Science Letters* 337-338, 47-55.

904 Eberl, D.D. (2003) User guide to RockJock - A program for determining quantitative mineralogy from X-ray
905 diffraction data.

906 Eberl, D.D. (2008) User's guide to HandLens—A computer program that calculates the chemistry of
907 minerals in mixtures.

908 Fletcher, R.C., Buss, H.L. and Brantley, S.L. (2006) A spheroidal weathering model coupling porewater
909 chemistry to soil thicknesses during steady-state denudation. *Earth and Planetary Science Letters*
910 244, 444-457.

911 Freyssinet, P. and Farah, A.S. (2000) Geochemical mass balance and weathering rates of ultramafic schists
912 in Amazonia. *Chem. Geol.* 170, 133-151.

913 Gioda, A., Mayol-Bracero, O.L., Scatena, F.N., Weathers, K.C., Mateus, V.L. and McDowell, W.H. (2013)
914 Chemical constituents in clouds and rainwater in the Puerto Rican rainforest: Potential sources and
915 seasonal drivers. *Atmospheric Environment* 68, 208-220.

916 Goldsmith, S.T., Carey, A.E., Johnson, B.M., Welch, S.A., Lyons, W.B., McDowell, W.H. and Pigott, J.S.
917 (2010) Stream geochemistry, chemical weathering and CO_2 consumption potential of
918 andesitic terrains, Dominica, Lesser Antilles. *Geochim. Cosmochim. Acta* 74, 85-103.

919 Goldsmith, S.T., Carey, A.E., Lyons, W.B. and Hicks, D.M. (2008) Geochemical fluxes and weathering of
920 volcanic terrains on high standing islands; Taranaki and Manawatu-Wanganui regions of New
921 Zealand. *Geochim. Cosmochim. Acta* 72, 2248-2267.

922 Graham, R.C., Rossi, A.M. and Hubbert, K.R. (2010) Rock to regolith conversion: Producing hospitable
923 substrates for terrestrial ecosystems. *GSA Today* 20, 4-9.

924 Hahm, W.J., Riebe, C.S., Lukens, C.E. and Araki, S. (2014) Bedrock composition regulates mountain
925 ecosystems and landscape evolution. *Proc. Natl. Acad. Sci. U. S. A.* 111, 3338-3343.

926 Heartsill-Scalley, T., Scatena, F.N., Estrada, C., McDowell, W.H. and Lugo, A.E. (2007) Disturbance and
927 long-term patterns of rainfall and throughfall nutrient fluxes in a subtropical wet forest in Puerto
928 Rico. *Journal of Hydrology* 333, 472-485.

929 Helgeson, H.C., Murphy, W.M. and Aagard, P. (1984) Thermodynamic and kinetic constraints on reaction
930 rates among minerals and aqueous solutions II. Rate constants, effective surface area, and the
931 hydrolysis of feldspar. *Geochim. Cosmochim. Acta* 48, 2405-2432.

932 Hillel, D. (1982) *Introduction to Soil Physics*. Academic Press, San Diego.

933 Jin, L., Ravella, R., Ketchum, B., Bierman, P.R., Heaney, P., White, T. and Brantley, S.L. (2010) Mineral
 934 weathering and elemental transport during hillslope evolution at the Susquehanna/Shale Hills
 935 Critical Zone Observatory. *Geochim. Cosmochim. Acta* 74, 3669-3691.

936 Jolly, W.T., Lidiak, E.G., Dickin, A.P. and Wu, T.-W. (1998) Geochemical diversity of Mesozoic island arc
 937 tectonic blocks in eastern Puerto Rico. *Geol. Soc. Am. Spec. Pap.* 322, 67-98.

938 Kesler, S.E. and Sutter, J.F. (1979) Chemical analysis of intrusive rocks from Puerto Rico. *Geological*
 939 *Society of America Suppl. Mater.* 79-5, 2 pp.

940 Köhler, S.J., Dufaud, F. and Oelkers, E.H. (2003) An experimental study of illite dissolution kinetics as a
 941 function of pH from 1.4 to 12.4 and temperature from 5 to 50°C. *Geochim. Cosmochim. Acta* 67,
 942 3583-3594.

943 Kump, L.R., Brantley, S.L. and Arthur, M.A. (2000) Chemical weathering, atmospheric CO₂ and climate.
 944 *Ann. Rev. of Earth and Planetary Sciences* 28, 611-667.

945 Kurtz, A.C., Lugolobi, F. and Salvucci, G. (2011) Germanium-silicon as a flowpath tracer: Application to the
 946 Rio Icacos watershed. *Water Resour. Res.* 47, W06516.

947 Larsen, M.C. (2012) Landslides and Sediment Budgets in Four Watersheds in Eastern Puerto Rico, in:
 948 Murphy, S.F., Stallard, R.F. (Eds.), *Water Quality and Landscape Processes of Four Watersheds in*
 949 *Eastern Puerto Rico: U.S. Geological Survey Professional Paper 1789*, pp. 153-178.

950 Liermann, L.J., Albert, I., Buss, H.L., Minyard, M. and Brantley, S.L. (2015) Relating Microbial Community
 951 Structure and Geochemistry in Deep Regolith Developed on Volcaniclastic Rock in the Luquillo
 952 Mountains, Puerto Rico. *Geomicrobiology* 32, 494-510.

953 Lugolobi, F., Kurtz, A.C. and Derry, L.A. (2010) Germanium-silicon fractionation in a tropical, granitic
 954 weathering environment. *Geochim. Cosmochim. Acta* 74, 1294-1308.

955 McClintock, M.A., Brocard, G., Willenbring, J., Tamayo, C., Porder, S. and Pett-Ridge, J.C. (2015) Spatial
 956 variability of African dust in soils in a montane tropical landscape in Puerto Rico. *Chem. Geol.* 412,
 957 69-81.

958 McDowell, W.H. and Asbury, C.E. (1994) Export of carbon, nitrogen, and major ions from three tropical
 959 montane watersheds. *Limnology and Oceanography* 39, 111-125.

960 Meybeck, M. (1987) Global chemical weathering of surficial rocks estimated from dissolved river loads.
 961 *Amer. J. Sci.* 287, 401-428.

962 Minyard, M.L., Bruns, M.A., Martinez, C.E., Liermann, L.J., Buss, H.L. and Brantley, S.L. (2011)
 963 Halloysite nanotubes and bacteria at the saprolite-bedrock interface, Rio Icacos Watershed, Puerto
 964 Rico. *Soil Sci Soc Am J* 75, 348-356.

965 Murphy, S.F., Brantley, S.L., Blum, A.E., White, A.F. and Dong, H. (1998) Chemical weathering in a
 966 tropical watershed, Luquillo Mountains, Puerto Rico; II. Rate and mechanism of biotite weathering.
 967 *Geochim. Cosmochim. Acta* 62, 227-243.

968 Murphy, S.F. and Stallard, R.F. (2012) Hydrology and climate of four watersheds in eastern Puerto Rico, in:
 969 Murphy, S.F., Stallard, R.F. (Eds.), *Water Quality and Landscape Processes of Four Watersheds in*
 970 *Eastern Puerto Rico: U.S. Geological Survey Professional Paper 1789*, pp. 43-83.

971 Navarre-Sitchler, A.K., Cole, D., Rother, G., Jin, L., Buss, H.L. and Brantley, S.L. (2013) Porosity and
 972 surface area evolution during weathering of two igneous rocks. *Geochim. Cosmochim. Acta* 109,
 973 400-413.

974 Parkhurst, D.L. and Appelo, C.A.J. (1999) User's guide to PHREEQC (Version 2)—A computer program for
 975 speciation, batch-reaction, one-dimensional transport, and inverse geochemical calculations, U.S.
 976 Geological Survey Water-Resources Investigations Report 99-4259, p. 310.

977 Pett-Ridge, J. (2009) Contributions of dust to phosphorus cycling in tropical forests of the Luquillo
 978 Mountains, Puerto Rico. *Biogeochemistry* 94, 63-80.

979 Pett-Ridge, J.C., Derry, L.A. and Kurtz, A.C. (2009) Sr isotopes as a tracer of weathering processes and dust
 980 inputs in a tropical granitoid watershed, Luquillo Mountains, Puerto Rico. *Geochim. Cosmochim.*
 981 *Acta* 73, 25-43.

982 Rad, S., Louvat, P., Gorge, C., Gaillardet, J. and Allègre, C.J. (2006) River dissolved and solid loads in the
 983 Lesser Antilles: New insight into basalt weathering processes. *Journal of Geochemical Exploration*
 984 88, 308-312.

985 Rad, S.D., Allegre, C.J. and Louvat, P. (2007) Hidden erosion on volcanic islands. *Earth Planet. Sci. Lett.*
 986 262, 109-124.

987 Richter, D.D. and Markewitz, D. (1995) How deep is soil? *Bioscience* 45, 600-609.

988 Riebe, C.S., Kirchner, J.W. and Finkel, R.C. (2003) Long-term rates of chemical weathering and physical
 989 erosion from cosmogenic nuclides and geochemical mass balance. *Geochim. Cosmochim. Acta* 67,
 990 4411-4427.

991 Scatena, F.N. (1989) An introduction to the physiography and history of the Bisley Experimental Watersheds
 992 in the Luquillo Mountains of Puerto Rico. USDA Forest Service, General Technical Report SO-72,
 993 p. 22.

994 Scatena, F.N., Silver, W., Siccama, T., Johnson, A. and Sanchez, M.J. (1993) Biomass and Nutrient Content
 995 of the Bisley Experimental Watersheds, Luquillo Experimental Forest, Puerto Rico, Before and After
 996 Hurricane Hugo. *Biotropica* 25, 15-27.

997 Schellekens, J., Bruijnzeel, L.A., Scatena, F.N., Bink, N.J. and Holwerda, F. (2000) Evaporation from a
 998 tropical rain forest, Luquillo Experimental Forest, eastern Puerto Rico. *Water Resour. Res.* 36, 2183-
 999 2196.

1000 Schellekens, J.H., Scatena, F.N., Bruijnzeel, L.A., van Dijk, A.I.J.M., Groen, M.M.A. and van Hogeand,
 1001 R.J.P. (2004) Stormflow generation in a small rainforest catchment in the Luquillo Experimental
 1002 Forest, Puerto Rico. *Hydrol. Process.* 18, 505-530.

1003 Schopka, H.H. and Derry, L.A. (2012) Chemical weathering fluxes from volcanic islands and the importance
 1004 of groundwater: The Hawaiian example. *Earth and Planetary Science Letters* 339-340, 67-78.

1005 Schulz, M.S. and White, A.F. (1999) Chemical weathering in a tropical watershed, Luquillo Mountains,
 1006 Puerto Rico; III. Quartz dissolution rates. *Geochim. Cosmochim. Acta* 63, 337-350.

1007 Seiders, V.M. (1971) Geologic map of the El Yunque quadrangle, Puerto Rico. U.S. Geological Survey.

1008 Silver, W.L., Scatena, F.N., Johnson, A.H., Siccama, T.G. and Sanchez, M.J. (1994) Nutrient availability in a
 1009 montane wet tropical forest: Spatial patterns and methodological considerations. *Plant Soil* 164, 129-
 1010 145.

1011 Simon, A., Larsen, M.C. and Hupp, C.R. (1990) The role of soil processes in determining mechanisms of
 1012 slope failure and hillslope development in a humid-tropical forest, eastern Puerto Rico.
 1013 *Geomorphology* 3, 263-286.

1014 Singh, R. and Gilkes, R.J. (1992) Properties of soil kaolinites from south-western Australia. *J. Soil. Sci.* 43,
 1015 645-667.

1016 Smith, A.L., Schellekens, J.H. and Diaz, A.M. (1998) Batholiths as markers of tectonic change in the
 1017 northeastern Caribbean. *Geol. Soc. Am. Spec. Pap.* 322, 99-122.

1018 Stallard, R.F. (2012) Weathering, Landscape Equilibrium, and Carbon in Four Watersheds in Eastern Puerto
 1019 Rico, in: Murphy, S.F., Stallard, R.F. (Eds.), *Water Quality and Landscape Processes of Four*
 1020 *Watersheds in Eastern Puerto Rico*. U.S. Geological Survey Professional Paper 1789-H, pp. 199-
 1021 247.

1022 Stallard, R.F. and Edmond, J.M. (1983) Geochemistry of the Amazon: 2. The influence of the geology and
 1023 weathering environment on the load. *Journal of Geophysical Research* 88, 9671-9688.

1024 Taylor, G. and Eggleton, R.A. (2001) *Regolith Geology and Geomorphology*. Wiley.

1025 Turner, B.F., Stallard, R.F. and Brantley, S.L. (2003) Investigation of in situ weathering of quartz diorite
 1026 bedrock in the Rio Icacos basin, Luquillo Experimental Forest, Puerto Rico. *Chem. Geol.* 202, 313-
 1027 341.

1028 USDA NCRS (2002) Soil Survey of Caribbean National Forest and Luquillo Experimental Forest,
 1029 Commonwealth of Puerto Rico. USDA, Natural Resources Conservation Service, Washington D.C.,
 1030 p. 181.

1031 Walker, T.W. and Syers, J.K. (1976) Fate of phosphorus during pedogenesis. *Geoderma* 15, 1-19.

1032 White, A.F. (2002) Determining mineral weathering rates based on solid and solute weathering gradients and
 1033 velocities: application to biotite weathering in saprolites. *Chem. Geol.* 190, 69-89.

1034 White, A.F. and Blum, A.E. (1995) Effects of climate on chemical weathering rates in watersheds. *Geochim.*
 1035 *Cosmochim. Acta* 59, 1729-1747.

1036 White, A.F., Blum, A.E., Schulz, M.S., Vivit, D.V., Stonestrom, D.A., Larsen, M., Murphy, S.F. and Eberl,
 1037 D. (1998) Chemical weathering in a tropical watershed, Luquillo Mountains, Puerto Rico: I. Long-
 1038 term versus short-term weathering fluxes. *Geochim. Cosmochim. Acta* 62, 209-226.

1039 White, A.F. and Brantley, S.L. (2003) The effect of time on the experimental and natural weathering rates of
 1040 silicate minerals. *Chem. Geol.* 202, 479-506.

1041 White, A.F. and Buss, H.L. (2014) 7.4 - Natural Weathering Rates of Silicate Minerals, in: Drever, J.I. (Ed.),
 1042 *Treatise on Geochemistry* (Second Edition). Elsevier, Oxford, pp. 115-155.

1043 White, A.F., Schulz, M.S., Lowenstern, J.B., Vivit, D. and Bullen, T.D. (2005) The ubiquitous nature of
 1044 accessory calcite in granitoid rocks: Implications for weathering and solute evolution, and
 1045 petrogenesis. *Geochim. Cosmochim. Acta* 69, 1455-1471.

1046 White, A.F., Schulz, M.S., Stonestrom, D.A., Vivit, D.V., Fitzpatrick, J., Bullen, T.D., Maher, K. and Blum,
 1047 A.E. (2009) Chemical weathering of a marine terrace chronosequence, Santa Cruz, California. Part
 1048 II: Solute profiles, gradients and the comparisons of contemporary and long-term weathering rates.
 1049 *Geochim. Cosmochim. Acta* 73, 2769-2803.
 1050 Wu, W., Hall, C.A.S., Scatena, F.N. and Quackenbush, L.J. (2006) Spatial modelling of evapotranspiration
 1051 in the Luquillo experimental forest of Puerto Rico using remotely-sensed data. *Journal of Hydrology*
 1052 328, 733-752.
 1053 Yi-Balan, S.A., Amundson, R. and Buss, H.L. (2014) Decoupling of sulfur and nitrogen cycling due to biotic
 1054 processes in a tropical rainforest. *Geochim. Cosmochim. Acta* 142, 411-428.
 1055 Ziegler, K., Chadwick, O.A., White, A. and Brzezinski, M.A. (2005) $\delta^{30}\text{Si}$ systematics in a granitic saprolite,
 1056 Puerto Rico. *Geology* 33, 817-820.
 1057

1058 **Figure Captions**

1059 **Figure 1.** Map of the Luquillo Critical Zone Observatory (LCZO) indicating the key lithological
1060 units. The approximate areas of the Río Icacos and Bisley 1 watersheds are shown as boxes on the
1061 large map as well as the site of the Río Icacos regolith profile LG1. The inset shows the watershed
1062 boundaries of the Bisley 1 and the hand-augered profile sites B1R, B1S(1-4), the borehole drilling
1063 sites B1W1 and B1W2 (Buss et al., 2013) and the USGS stream gage.

1064 **Figure 2.** Si and Mg pore water solute concentrations with depth in the LCZO ridgetop sites. (a)
1065 and (b) Measured Si concentrations (open symbols) in Bisley pore waters, with net weathering
1066 concentrations (closed symbols) calculated from the averages of the study period (Eq. 4). (c)
1067 Average net Si weathering concentrations for site LG1, taken from Schulz and White (1999). (d)
1068 and (e) Measured Mg concentrations (open symbols) in Bisley pore waters, with net weathering
1069 concentrations (closed symbols) calculated from the averages over the study period (Eqn. 4). (f)
1070 Average net Mg weathering concentrations for site LG1, taken from Schulz and White (1999).
1071 Note different scale on depth axis for site B1R (a and d). Dashed lines indicate linear gradients
1072 used to calculate short-term solute fluxes (Eq. 11, Tables 9-10). The LG1 gradients were
1073 determined by (c) Schulz and White (1999) and (f) White (2002). Error bars on Bisley data
1074 indicate the standard error of the average for the measured concentrations, which was propagated
1075 for the net concentrations. Only mean values were available for the LG1 site (Schulz and White,
1076 1999; White, 2002).

1077 **Figure 3.** Average pore space concentrations of gaseous (a) CO₂ and (b) O₂. For comparison,
1078 average atmospheric concentrations are: O₂ 20.9% and CO₂ 0.039%. Error bars are the standard
1079 error of the average of 2-4 sampling dates during different seasons (B1S1 and B1R). LG1 gas
1080 samplers were installed last and data reflect only one sampling date, with error bars representing
1081 standard error of the mean of repeat measurements on the same samples.

1082 **Figure 4.** Oxide wt.% (symbols) and major mineralogy (shaded areas) for site B1R (a-d) and B1S1
1083 (e-h). Note different scales for different oxides and minerals. Chlorite was not detected in site B1R.
1084 Al content corresponds to kaolinite (a, e) except between 1-4 m depth at site B1R where the trends
1085 diverge. Si, Fe(total), and Mg can be correlated with quartz (b, f), Fe-(hydr)oxides (goethite and
1086 hematite, c, g), and chlorite (d, h), respectively.

1087 **Figure 5.** Assessment of Zr (a-c) and Ti (d-f) immobility. The horizontal line is the mean of the
1088 range of bedrock composition values $\pm 1\sigma$ (dotted lines). Open circles = samples that overlap the
1089 $\pm 1\sigma$ zones, closed circles = samples that do not overlap the $\pm 1\sigma$ zones. (a) B1R: Samples that do not

1090 overlap the $\pm 1\sigma$ zone: 14.9 and 15.4 m. **(b)** B1S1: Samples that do not overlap the $\pm 1\sigma$ zone: 0.6,
1091 1.2-2.4, and 9.0 m. Samples that do overlap the $\pm 1\sigma$ zone: 0.9, 3.3-8.5, and 9.3 m. **(c)** LG1: All
1092 samples overlap the $\pm 1\sigma$ zone. **(d)** B1R: Samples that do not overlap the $\pm 1\sigma$ zone: 0.6, 0.8, 2.3-6.9,
1093 8.9-10.1, 13.1-14.9, 15.7-15.9 m. Samples that do overlap the $\pm 1\sigma$ zone: 0.04-0.35, 1.3, 7.4-8.5,
1094 11.3-12.2, 15.4 m. **(e)** B1S1: Most samples do not overlap the $\pm 1\sigma$ zone; those that do overlap: 4.9
1095 and 7.6 m. **(f)** LG1: Samples that do not overlap the $\pm 1\sigma$ zone: 0.25 m.

1096 **Figure 6.** Volumetric strain with depth in the ridgetop sites. Error bars reflect estimated 3% error on
1097 bulk density measurements, detection limits of elemental analyses and SE of the mean parent Zr
1098 concentrations, propagated through the calculation. **(a)** Strain values near zero indicate near
1099 isovolumetric weathering at Bisley site B1R with slight dilation in B1R, particularly near 2.5 and 7
1100 m depth. and **(b)** near isovolumetric weathering throughout Bisley site B1S1. **(c)** Strain in Rio
1101 Icos site LG1 indicates modest dilation at most depths.

1102 **Figure 7.** Ridgetop mass transfer (τ) profiles for inorganic nutrient elements: K **(a-e)**, P **(f-j)**, and
1103 Mg **(k-o)**. Sites are arranged in columns, from left to right: B1R, B1S1, B1S2, B1S4, LG1 for each
1104 row and exclude the weathered clasts recovered in some profiles. Note different depth (y-axis) scale
1105 for B1R (first column) and different τ (x-axis) scales for (a, e, and f). Na and Ca (not shown) are
1106 completely depleted ($\tau_{j,Zr} = -1$) in almost every sample of every profile, with the exception of
1107 B1S4, where $\tau_{Na,Zr} = -0.5$ at the bottom (0.9 m depth). Vertical solid lines (a, e, f) indicate $\tau = 0$.
1108 Dashed lines in some profiles indicate linear gradients used to calculate long-term elemental fluxes
1109 (Eq. 10, Table 9). The gradient used to calculate the long-term chlorite weathering rate (Eq. 8,
1110 Tables 9-10) is not shown, but determined from data in (l) from 8.2-9.3 m depth only.

1111 **Figure 8.** Mass transfer (τ) profiles of less-mobile elements: j = Si (circles) or Fe (triangles). Note
1112 different depth and τ scales were used to show key features. Solid vertical lines indicate $\tau = 0$.
1113 **(a-d)** All Bisley profiles are depleted in Si and Fe reflecting extreme mass loss due to chemical
1114 weathering. However, the deeper ridgetop profiles (a-b, B1R and B1S1) indicate some enrichment
1115 of Fe, suggesting redistribution occurs over time. Dashed lines in B1S1, B1S2 and B1S4 profiles **(b,**
1116 **c, d)** indicate linear gradients used to calculate long-term Si fluxes (Eq. 10, Table 9). Weathered
1117 clasts are excluded from these profiles. **(e)** Si enrichment occurs at the surface of Río Icos site
1118 LG1, which may reflect biogenic input of Si as phytoliths (Ziegler et al., 2005; Lugolobi et al.,
1119 2010). Error was calculated from the analytical detection limits and standard errors of the mean
1120 parent rock compositions (Table 2) and propagated through the calculations. Error bars for Si are
1121 smaller than the symbols and Fe error bars are not shown for clarity.

1122

1123 **Figure 9.** Net solute concentrations in B1R pore waters versus ammonium-acetate extractable Mg.
1124 (a) Net Mg concentrations and (b) net Si concentrations both correlate well with extractable Mg
1125 below the shallowest depths, where extractable Mg is much higher than in the remainder of the
1126 profile.

1127 **Figure 10.** Mass transfer (τ) profiles of clay minerals in the B1S1 profile. (a) Kaolinite increases
1128 from the bottom of the profile to about 4.9 m depth, above which a depletion trend is evident. (b)
1129 Illite increases from the bottom only to about 7.6 m depth; a depletion trend extends from this depth
1130 to the surface. Both profiles are consistent with secondary clay formation during earlier stages of
1131 weathering followed by dissolution in the upper meters of the regolith. Dashed lines indicate linear
1132 gradients used for calculating long-term mineral dissolution rates (Eq. 8, Tables 9-10). Error bars
1133 reflect XRD detection limits and standard error of the mean parent rock compositions, propagated
1134 through the calculations.

1135

Table 1. Regolith physical properties

Depth	Water	Bulk	
(m)	Content ^a	Density	Porosity
	(vol %)	(g cm ⁻³)	(%)
B1R (Upper Ridge)			
0.05	31.7	0.89	66
0.29	25.5	1.25	53
0.36	15.8	1.38	48
0.58	19.2	1.47	45
0.79	16.5	1.67	37
1.42	21.3	1.55	42
2.43	20.7	1.48	44
3.06	19.7	1.49	44
3.80	17.5	1.57	41
5.00	15.3	1.42	46
B1S1 (Lower Ridge)			
0.30	35.2	0.95	64
0.61	25.8	1.19	55
0.91	27.4	1.18	56
1.22	26.6	1.18	55
1.52	28.4	1.13	57
1.83	29.4	1.11	58
2.44	32.0	1.05	60
3.30	29.9	1.07	60
3.66	32.2	1.05	61
4.27	33.3	0.99	63
4.88	32.2	1.01	62
5.49	30.4	1.00	62
6.10	32.5	1.01	62
6.71	32.1	1.06	60

^a Gravimetric water content, bulk density and porosity approximately ± 3% of the values given, based on replicate analyses.

Table 2. Solid-state elemental concentrations^a of rocks and regolith

Depth	Al ₂ O ₃	CaO	Fe ₂ O ₃	FeO ^b	K ₂ O	MgO	MnO	Na ₂ O	P ₂ O ₅	SiO ₂	TiO ₂	Nb	Sr	Zn	Zr
(m)	(wt. %)		<i>total Fe</i>									(ppm)			
Bisley Bedrock^c															
	16.8	7.9	8.6	6.1	0.8	5.5	0.15	2.8	0.11	53.1	0.65	<10	540	77	82
	±0.3	±0.5	±0.2	±0.3	±0.1	±0.3	±0.02	±0.2	±0.01	±0.7	±0.02		±40	±4	±4
Rio Icos Bedrock^c															
	17.0	7.32	8.5	4.6	0.86	2.9	0.17	3.0	0.12	55.3	0.58	<10	247	-	85
	±0.6	±0.06	±0.7	±0.4	±0.03	±0.3	±0.02	±0.1	±0.01	±0.5	±0.04		±9	-	±3
B1R Regolith															
0.04	16.2	0.11	8.32	0.20	0.30	0.18	<0.01	0.14	0.07	53.6	0.87	40	40	28	120
0.2	17.5	0.09	9.66	0.20	0.33	0.17	<0.01	0.24	0.06	56.6	0.92	40	30	35	130
0.4	18.0	0.03	10.4	0.10	0.42	0.18	<0.01	0.20	0.05	57.7	0.94	50	30	27	130
0.6	13.7	0.02	6.29	0.20	1.34	0.33	<0.01	0.24	0.05	65.0	0.61	70	30	23	90
0.8	13.1	0.03	28.9	0.10	1.21	0.30	0.03	0.22	0.65	40.5	0.52	70	20	197	90
1.3	18.7	0.03	10.8	<0.1	0.48	0.11	0.02	0.17	0.22	59.4	0.81	50	30	86	110
2.3	19.6	0.03	9.16	<0.1	0.71	0.15	0.02	0.17	0.21	60.5	0.79	40	30	59	70
3.1	20.4	0.02	9.43	<0.1	0.55	0.13	0.04	0.22	0.16	60.4	0.90	30	40	51	150
3.5	14.7	0.03	18.0	<0.1	1.29	0.26	0.08	0.20	0.52	55.6	0.47	30	30	84	90
3.7	14.1	0.03	5.51	<0.1	1.55	0.33	0.02	0.19	0.20	71.5	0.64	30	110	37	110
5.0	17.6	0.02	8.42	<0.1	0.91	0.18	0.03	0.17	0.25	63.6	0.89	20	30	52	200
5.6	18.6	0.03	7.09	<0.1	0.73	0.18	0.08	0.06	0.21	63.3	0.75	10	60	30	140
6.2	22.1	0.01	9.98	<0.1	0.31	0.10	0.11	0.04	0.17	53.9	0.83	20	20	35	130
6.9	11.5	0.04	4.60	<0.1	0.41	0.10	0.03	0.08	0.08	75.5	0.39	<10	10	22	70
7.4	8.74	0.02	7.51	<0.1	0.46	0.10	0.14	0.20	0.13	76.9	0.37	40	20	31	50
7.6	11.0	0.05	5.07	<0.1	0.60	0.16	0.03	0.04	0.09	75.4	0.51	10	30	14	70
8.5	19.2	0.17	9.43	<0.1	0.16	0.15	0.07	0.11	0.10	60.6	0.70	<10	10	23	80
8.9	24.2	0.02	12.1	<0.1	0.14	0.08	0.46	0.12	0.13	51.5	0.84	40	<10	55	80
9.3	24.5	0.02	13.7	<0.1	0.15	0.12	0.70	0.02	0.16	45.3	0.92	20	<10	69	90
10.1	22.8	0.02	11.3	<0.1	0.18	0.08	0.14	0.12	0.14	51.3	0.91	40	<10	37	90
11.3	17.8	0.02	8.88	<0.1	0.58	0.15	0.10	0.14	0.18	64.5	0.88	50	20	41	110
12.2	18.7	0.10	19.5	<0.1	0.41	0.15	0.51	0.03	0.25	48.2	0.83	20	<10	73	110
13.1	15.5	0.02	8.57	<0.1	0.53	0.15	0.10	0.12	0.15	66.0	0.75	40	10	30	120
14.3	22.6	0.02	13.8	<0.1	0.32	0.11	0.19	0.13	0.15	51.3	0.86	40	<10	37	130
14.9	24.8	0.02	11.3	<0.1	0.45	0.11	0.17	<0.01	0.14	49.5	0.93	30	40	55	280

15.4	17.7	0.03	13.5	<0.1	0.82	0.17	0.53	0.13	0.20	55.7	0.62	50	30	79	120
15.5	16.7	0.03	13.8	<0.1	0.46	0.11	0.59	0.12	0.23	53.8	0.54	40	30	94	100
15.7	22.5	0.01	8.69	<0.1	0.36	0.10	0.57	<0.01	0.13	54.9	0.90	30	30	66	180
15.8	21.3	0.02	9.47	<0.1	0.30	0.07	0.41	0.15	0.13	54.9	0.80	30	20	67	140
15.9	19.3	0.05	11.4	<0.1	0.22	0.09	0.24	<0.01	0.17	56.8	0.94	20	10	51	160
B1R Augered Clasts															
5.6	16.7	0.07	5.89	-	0.59	0.15	0.05	0.01	0.16	67.2	0.51	20	40	28	80
6.2	23.2	0.01	8.23	-	0.29	0.09	0.10	0.01	0.15	55.3	0.91	30	20	32	130
6.9	5.47	0.05	2.89	-	0.30	0.07	<0.01	<0.01	0.05	76.4	0.28	20	30	7	60
7.6	8.27	<0.01	3.69	-	0.53	0.13	0.02	<0.01	0.07	76.5	0.39	<10	20	7	60
8.5	20.5	0.02	9.50	-	0.08	0.06	0.10	<0.01	0.11	58.5	0.74	10	<10	34	90
9.3	25.3	<0.01	12.4	-	0.22	0.12	1.04	<0.01	0.19	46.2	0.86	20	<10	73	90
12.2	24.4	0.01	11.6	-	0.17	0.07	0.05	<0.01	0.21	48.5	1.11	30	<10	28	150
14.9	25.7	<0.01	10.8	-	0.56	0.12	0.02	0.02	0.14	46.5	0.99	30	40	45	390
15.9	22.3	0.01	9.51	-	0.24	0.06	0.14	0.05	0.15	54.2	0.78	20	10	62	130
15.7	23.2	0.01	8.73	-	0.39	0.10	0.74	<0.01	0.15	52.8	0.97	20	30	67	180
B1S1 Regolith															
0.6	22.9	0.02	11.3	-	0.07	0.29	0.02	<0.1	0.08	46.5	1.03	20	4.0	53	210
0.9	22.0	0.03	11.1	-	0.06	0.29	0.03	<0.1	0.09	57.2	0.92	10	2.1	41	170
1.2	22.5	0.01	11.2	-	0.07	0.23	0.02	<0.1	0.10	54.7	0.89	20	2.4	39	170
1.5	21.8	0.01	9.83	-	0.05	0.24	0.02	<0.1	0.10	55.5	0.84	10	2.2	37	170
1.8	23.7	0.02	10.7	-	0.04	0.45	0.03	<0.1	0.06	46.5	0.93	10	1.0	38	180
2.7	23.6	0.02	11.1	-	0.12	0.48	0.04	<0.1	0.09	48.3	0.95	20	1.0	45	180
3.1	26.0	<0.01	11.8	-	0.12	0.53	0.05	<0.1	0.09	45.9	1.03	10	<10	63	170
3.7	24.0	0.01	11.2	-	0.17	0.51	0.08	<0.1	0.08	49.5	0.95	<10	<10	48	160
4.3	22.1	0.03	10.8	-	0.10	0.54	0.21	<0.1	0.07	52.3	0.85	<10	1.4	59	150
4.9	23.8	0.02	12.2	-	0.08	0.62	0.40	<0.1	0.08	49.7	0.91	10	<10	67	130
5.5	23.1	0.02	11.6	-	0.07	0.60	0.46	<0.1	0.06	48.9	0.87	10	<10	72	130
6.4	22.0	0.01	11.1	-	0.15	0.61	0.24	<0.1	0.07	47.2	0.84	<10	1.9	62	130
7.0	23.2	0.03	11.6	-	0.24	0.81	0.42	<0.1	0.07	48.1	0.87	<10	<10	78	130
7.6	22.1	0.01	10.9	-	0.32	0.77	0.38	<0.1	0.07	47.6	0.82	<10	<10	71	120
8.2	24.1	0.01	11.4	-	0.17	0.80	0.24	<0.1	0.05	46.0	0.93	10	2.2	79	150
8.5	21.1	0.02	8.36	-	0.22	0.66	0.25	<0.1	0.06	52.9	0.73	<10	<10	79	130
9.0	19.1	0.02	8.85	-	0.44	0.89	0.26	<0.1	0.09	57.9	0.74	<10	<10	123	140
9.3	20.7	0.03	9.85	-	0.69	1.42	0.37	<0.1	0.12	51.4	0.73	10	17	172	120

B1S1 Augered Clasts

0.6	5.47	0.02	9.57	-	0.04	0.04	<0.01	<0.1	0.09	74.3	0.74	<10	<10	37	150
4.3	6.40	0.05	4.79	-	0.19	0.10	0.02	<0.1	0.09	76.7	0.33	<10	<10	16	80
9.0	6.32	0.09	3.36	-	0.76	0.88	0.06	0.1	0.07	83.1	0.37	<10	30	51	80
9.3	7.49	0.03	4.99	-	0.92	1.16	0.06	<0.1	0.06	75.4	0.59	<10	34.5	84	100

B1S2 Regolith

0.15	19.7	0.02	10.4	-	0.07	0.41	0.02	<0.1	0.07	48.5	0.99	20	<10	41	150
0.6	21.7	0.01	10.8	-	0.59	0.99	0.43	0.1	0.09	49.0	0.88	20	10	92	120
0.9	23.1	0.01	11.6	-	0.11	0.41	0.04	<0.1	0.12	46.6	1.06	20	<10	57	180
1.5	23.5	0.03	10.5	-	0.19	1.41	0.40	<0.1	0.10	47.1	0.94	20	<10	153	140
1.8	23.4	<0.01	11.5	-	0.24	0.95	0.65	<0.1	0.09	46.1	0.98	20	<10	101	150
2.7	22.6	0.02	11.0	-	0.36	2.22	0.31	0.2	0.12	46.2	0.97	20	10	297	140

B1S2 Augered Clasts

0.6	7.74	0.04	6.05	-	0.21	1.84	0.06	<0.1	0.10	76.5	0.76	20	20	75	140
-----	------	------	------	---	------	------	------	------	------	------	------	----	----	----	-----

B1S3 Regolith

0.15	22.5	0.02	11.2	-	0.16	0.81	0.25	<0.1	0.08	47.7	0.93	20	<10	77	130
1.2	21.7	0.01	11.1	-	0.48	1.32	0.39	0.1	0.10	48.3	0.89	20	10	166	120

B1S4 Regolith

0.15	20.2	0.09	11.0	-	0.16	0.79	0.25	<0.1	0.09	45.9	0.91	20	10	89	130
0.3	19.3	0.13	9.60	-	0.67	1.66	0.21	1.0	0.09	51.9	0.83	20	50	120	130
0.9	15.4	0.53	6.99	-	1.29	1.77	0.10	1.4	0.09	62.1	0.67	20	90	97	120

LG1 Regolith

0.15	13.2	0.03	4.74	-	0.27	0.13	0.02	<0.01	0.01	68.3	0.36	<10	<10	-	138
0.3	12.7	0.03	4.30	-	0.27	0.11	0.02	0.02	<0.01	69.0	0.34	<10	<10	-	189
0.5	15.7	0.02	5.12	-	0.34	0.19	0.02	<0.01	<0.01	65.1	0.43	<10	<10	-	145
0.6	19.4	0.06	6.46	-	0.60	0.48	0.07	0.03	0.01	60.9	0.47	<10	<10	-	167
0.8	17.1	0.03	5.79	-	0.56	0.44	0.07	0.03	0.01	62.4	0.42	<10	<10	-	99
0.9	20.6	0.02	6.75	-	0.74	0.53	0.31	0.02	0.04	57.2	0.44	<10	<10	-	107
1.1	20.6	0.02	6.67	-	0.92	0.72	0.08	0.02	0.02	57.6	0.46	<10	<10	-	183
1.2	18.3	0.03	6.31	-	0.84	0.64	0.08	0.02	0.04	58.7	0.45	<10	<10	-	94
1.4	20.2	0.02	7.23	-	0.84	0.67	0.17	0.02	0.04	57.7	0.47	<10	<10	-	97
1.5	20.6	0.03	7.39	-	0.82	0.67	0.08	<0.01	0.03	58.5	0.50	<10	<10	-	103
1.8	19.7	0.07	6.63	-	0.90	0.53	0.05	0.04	0.04	61.5	0.42	<10	<10	-	101
2.1	21.0	0.02	6.47	-	0.91	0.46	0.06	<0.01	0.03	58.5	0.48	<10	<10	-	106
2.4	24.4	0.02	5.66	-	0.77	0.51	0.46	<0.01	0.05	54.6	0.39	<10	<10	-	80

2.7	22.5	0.02	6.91	-	0.91	0.66	0.13	0.01	0.07	57.9	0.46	<10	<10	-	113
3.0	23.8	0.05	7.43	-	1.03	0.74	0.06	0.07	0.06	57.3	0.49	<10	<10	-	132
3.4	20.4	0.02	6.66	-	1.09	0.70	0.09	0.06	0.04	59.2	0.45	<10	<10	-	120
3.7	20.4	0.02	6.99	-	1.00	0.61	0.12	0.03	0.03	57.8	0.46	<10	<10	-	103
4.0	19.4	0.02	7.23	-	1.07	0.63	0.12	0.03	0.02	58.5	0.47	<10	<10	-	129
4.3	18.2	0.03	6.90	-	1.03	0.55	0.26	0.07	0.02	59.4	0.44	<10	<10	-	128
4.6	20.6	0.04	8.26	-	0.98	0.61	0.295	0.05	0.04	55.4	0.56	<10	<10	-	101
4.9	18.7	0.89	6.78	-	1.41	1.29	0.255	0.61	0.09	60.1	0.43	<10	28	-	97
5.2	16.6	2.52	6.13	-	1.34	1.52	0.17	1.67	0.08	61.3	0.39	<10	92	-	138
5.5	16.7	2.59	6.32	-	1.45	1.95	1.03	1.74	0.07	60.0	0.42	<10	85	-	98
5.8	15.7	3.74	5.42	-	1.47	1.73	0.13	2.43	0.08	63.3	0.37	<10	143	-	75
6.1	15.4	3.55	5.09	-	1.45	1.57	0.14	2.36	0.08	60.5	0.36	<10	140	-	115
6.4	16.3	4.02	4.90	-	1.47	1.59	0.13	2.69	0.08	63.7	0.34	<10	159	-	66
6.7	15.4	4.06	5.52	-	1.50	1.84	0.15	2.53	0.08	63.7	0.38	<10	153	-	62
7.0	15.2	3.94	5.52	-	1.53	1.79	0.15	2.54	0.07	65.2	0.37	<10	150	-	81
7.3	16.6	4.48	5.57	-	1.35	1.92	0.18	2.67	0.10	59.9	0.36	<10	162	-	111

^a Detection limits = 0.01 wt % for Al₂O₃, CaO, Fe₂O₃, K₂O, MgO, MnO, Na₂O (B1R), P₂O₅, SiO₂, and TiO₂; 0.1 wt% Na₂O (B1S1-4); 10 ppm for Nb, Sr, Zn; 5 ppm for Zr.

^b Ferrous iron was not analysed for sites B1S1-4.

^c Averaged bedrock data includes \pm SE of the mean.

Table 3. Concentrations of cations in NH₄-acetate extracts

Depth (m)	Al (mmol kg ⁻¹)	Ca	K	Mg	Na	Sr
DL^a	0.0025	0.05	0.1	0.03	0.01	4x10 ⁻⁶
B1R regolith						
0.04	0.069	4.61	1.0	3.52	2.49	0.0176
0.2	0.023	1.58	0.7	1.63	1.34	0.0088
0.4	0.013	0.84	0.4	1.47	0.88	0.0053
0.8	0.008	0.38	0.3	0.37	0.40	0.0020
1.3	0.206	0.27	bd	0.33	0.61	0.0025
2.3	0.010	0.20	0.1	0.41	0.94	0.0022
3.1	0.008	0.14	0.1	0.66	1.34	0.0034
3.7	0.015	0.21	0.4	0.46	0.60	0.0010
5.0	0.010	0.27	0.2	0.48	1.78	0.0027
5.6	0.004	0.04	0.1	0.45	1.00	0.0013
6.2	0.001	0.08	0.2	0.65	0.88	0.0013
6.7	bd	0.05	bd	0.42	0.62	0.0011
6.9	0.016	0.10	0.1	0.22	0.40	0.0030
7.4	bd	0.10	0.1	0.16	0.36	0.0011
7.6	bd	0.14	0.1	0.27	0.48	0.0018
7.7	bd	0.05	bd	0.21	5.00	0.0012
8.4	0.005	0.10	bd	0.41	0.47	0.0017
8.9	0.000	0.05	0.1	0.78	0.64	0.0026
9.2	0.024	0.16	0.5	1.28	0.92	0.0036
10.1	0.007	0.13	bd	0.71	0.76	0.0020
11.3	0.013	0.14	0.3	0.60	0.51	0.0015
12.2	0.000	0.21	0.3	0.78	0.66	0.0017
13.1	bd	0.09	0.2	0.53	0.32	0.0010
14.3	0.006	0.11	0.2	0.99	0.50	0.0014
14.9	bd	0.09	0.1	0.56	1.01	0.0026
15.4	0.006	0.17	0.1	0.72	0.70	0.0016
15.5	0.001	0.04	0.2	0.72	0.89	0.0016
15.7	0.002	0.13	0.1	0.65	0.98	0.0015
15.8	bd	0.08	0.1	0.62	1.29	0.0019
15.9	0.012	0.11	0.1	0.70	1.59	0.0024
B1S1 regolith						
0.6	0.03	0.41	0.2	1.47	0.60	0.0024
1.8	0.05	0.32	0.4	1.19	0.53	0.0011
3.1	0.06	0.37	0.7	1.30	0.84	0.0013
4.3	0.09	0.38	0.5	1.48	0.72	0.0011
4.9	0.05	0.36	0.7	1.66	0.76	0.0011
5.5	0.07	0.42	0.3	1.91	0.78	0.0016
6.4	0.05	0.37	0.6	2.69	0.88	0.0017
7.0	0.17	0.37	1.0	3.88	0.97	0.0020
7.6	0.19	0.38	1.1	4.13	1.03	0.0020
8.2	0.17	0.34	1.2	6.65	1.31	0.0033
8.5	0.06	0.38	1.0	7.13	1.35	0.0046
9.0	0.06	0.57	1.2	6.87	1.17	0.0048
9.3	0.06	0.61	1.3	10.1	1.27	0.0088

^aDL=detection limit

Table 4. Average pore water concentrations^a

Depth (m)	pH(calc) ^b	Na (uM)	Mg	Al	Si	K	Ca	Sr	Cl	SO4	NO3
B1R pore water											
0.15	4.5	285±8	36±6	2.3±0.5	240±10	11±1	36±6	0.19±0.03	320±10	7±1	130±40
0.3	4.6(5.3)	390±20	30±3	3.3±0.6	180±10	11±1	14±2	0.108±0.006	400±20	13±45	100±20
0.6	4.5(4.7)	280±10	25±1	2.6±0.5	166±7	5±1	12±2	0.060±0.005	260±10	19±4	80±20
0.9	4.4(4.6)	245±5	30±1	4.2±1.0	144±6	5±1	9±2	0.050±0.003	227±8	22±4	84±8
1.2	4.4	223±3	30±1	4.4±0.7	128±6	5±1	14±1	0.072±0.004	233±5	23.9±0.3	63±4
1.5	4.5(4.6)	207±5	34.3±0.5	6±1	121±6	3.9±0.7	13±1	0.075±0.003	229±1	29.6±0.7	56±2
1.8		196±7	29.7±0.7	5.9±0.9	131±1	4±1	12±1	0.057±0.003	209±8	22±1	63±9
2.4	4.8	191±6	32±1	3.6±0.8	174±8	1.4±0.5	19±2	0.104±0.009	231±9	21±2	31±4
3.4	4.6(4.6)	200±10	30±2	4 ±1	170±9	3.2±0.7	11±2	0.063±0.002	230±20	20±2	33±4
4.9		260±30	36±2	3.4±0.8	170±20	2.3±0.6	23±2	0.057±0.008	290±40	22±2	60±30
5.8		290±40	37±3	3 ±1	180±20	2.8±0.6	18±2	0.060±0.006	330±50	20±3	17±2
6.4	4.7(4.6)	260±5	41.2±0.6	6±1	191±6	2.4±0.4	12±2	0.073±0.004	318±9	16±1	37±3
16.0		280±20	50±1	4±1	210±5	7±3	12±1	0.060±0.005	370±20	17.6±0.4	24±3
B1R openfall (volume weighted average)											
	5.1-7.0	120±20	11±2	0.5±0.2	2.1±0.3	3.3±0.6	8±1	0.029±0.003	140±20	17±2	bd
B1S1 pore water											
0.15	4.89	102±7	13±27	0.7±0.2	170±20	6.9±0.7	4 ±1	0.074±0.009	128±3	12±2	9±5
0.3	4.4	185±2	34±1	6.3±0.9	149±7	6 ±2	4.4±0.9	0.085±0.002	310±4	1.0±0.3	5±3
0.6	4.8(4.7)	110±5	19.8±0.7	2.9±0.8	91±7	6±3	4.0±0.7	0.033±0.002	164±7	4.3±0.7	6±4
0.9	4.6	131±3	23.5±0.3	6.5±0.7	97±6	4±1	2.5±0.9	0.044±0.001	214±4	4.6±0.7	4±2
1.2	4.7	111±4	14.8±0.4	6.0±0.8	88±7	4±1	4±3	0.033±0.002	152±1	10.7±0.2	3±1
1.5	4.5	154±5	32±1	10±1	87±4	5±2	3±1	0.047±0.003	300±2	2.8±0.1	1.2±0.3
1.8	4.6(3.9)	98±4	17.2±0.6	5.8±0.5	51±6	4.0±1.0	4±1	0.040±0.001	138±6	27.5±0.9	0.7±0.2
4.3	4.7(4.5)	196±9	36±1	6.7±0.3	101±5	0.2±0.2	3±1	0.033±0.001	306±1	3±0.4	6.9±0.5
9.3	5.4	257±4	36±1	1.3±0.4	184±4	11.9±0.7	4±1	0.046±0.001	297±3	7.4±0.8	11.8±0.6
B1S2 pore water											
0.15	4.55	240±10	24±3	2.3±0.5	250±20	7.5±0.6	4.5±0.8	0.048±0.006	250±20	21±5	12±4
0.3	4.7	300±20	19±2	2.0±0.8	210±20	10±1	5±2	0.037±0.004	320±20	23±3	4±2
0.9	5.2	260±20	12.3±0.4	0.11±0.6	113±5	5.8±0.7	2±2	0.028±0.007	244±8	14±4	4±3
1.2	5.1	280±10	12.8±0.4	0.4±0.1	106±9	4.2±0.7	1.2±0.4	0.019±0.001	280±10	14.4±0.8	5±3
1.5	5.3	311±9	12.7±0.5	0.5±0.2	110±10	4.3±0.9	0.7±0.4	0.019±0.001	306±7	15.7±0.1	6±2

1.8	5.3	240±10	16±3	1±1	106±3	5.2±0.8	4±1	0.034±0.004	233±9	21±3	10±1
2.7	5.4	225±5	12.7±0.2	0.4±0.1	133±6	2.4±0.7	4±1	0.032±0.001	217±2	9±1	14±3
B1S3 pore water											
0.15	4.6	390±50	90±10	1.5±0.6	184±7	12±4	39±5	0.29±0.04	740±60	6±3	1.1±0.7
0.3	4.8	540±70	110±20	0.4±0.2	160±10	8±1	40±6	0.33±0.05	970±50	1.3±0.3	3±2
0.6	5.6	83±6	4±1	0.06±0.03	130±10	3±1	1.1±0.4	0.013±0.001	25±6	10±1	12±6
0.9	5.2	145±7	18±3	0.17±0.6	123±5	1.2±0.8	0.3±0.3	0.019±0.002	150±10	12.2±0.7	2±1
1.5	5.7	123±6	10±2	0.9±0.6	128±4	4±1	0.8±0.5	0.020±0.001	66±6	23.3±0.7	6±2
B1S4 pore water											
0.15	5.7	175±6	55±3	0.2±0.1	199±6	17±2	32±2	0.216±0.008	241±5	15.1±0.8	2±1
0.3	5.6	176±5	36±1	0.13±0.06	188±5	9.5±0.4	19±1	0.144±0.006	169±4	14±1	15±4
0.6	5.7	231±7	43±2	0.06±0.05	260±8	17.2±0.6	8±1	0.117±0.004	193±1	24.3±0.7	8±3
0.9	5.6	201±6	46±4	0.2±0.1	179±7	11.4±1	14±1	0.120±0.005	184±9	16±1	29±6

^aPore water concentrations for each sample averaged over time ± SE of the mean.

^bpH values as measured in pore water, pH in parentheses were calculated from pCO₂ using PHREEQCi (Parkhurst and Appelo, 1999).

Table 5. Average bedrock mineralogy by quantitative XRD^a

Quartz (wt. %)	K-spar ^b	Plag ^b	Kaolinite	Chlorite	Pyroxene	Amphibole ^c	Calcite	Epidote	Prehnite	Illite ^c
10±1	5.8±0.9	36±1	0.4±0.1	24±1	9.4±0.9	3.6±0.3	0.8±0.3	8±2	2±1	.9±0.3

^a Bedrock XRD data from Buss et al. (2013) ± SE of the mean.

^b K-spar = orthoclase, Plag = plagioclase

^c Amphibole was previously identified as tourmaline and illite was previously identified as biotite (Buss et al., 2013). Subsequent extensive thin section analysis (optical and SEM) has identified only amphibole and illite.

Table 6. Precipitation and pore water fluxes (m yr⁻¹), Cl concentrations (μM) and hydrologic parameters

Site	Precip. Cl (μM)	Deep pore water Cl (μM)	Precip. Flux, q _{precip} (m y ⁻¹)	Pore water flux density, q _p (m y ⁻¹)	Average porosity, Φ (m ³ m ⁻³)	Average saturation, Γ (m ³ m ⁻³)	Infiltration rate, I (m yr ⁻¹)	Fluid residence time (yr)
B1R ^a	150±20	320±17	3.4±0.2	1.5±0.3	0.47±0.02	0.62±0.04	5.3±0.3	1.8±0.1
B1S1 ^a	150±20	303±2	3.4±0.2	1.6±0.2	0.60±0.08	0.55±0.07	5.0±0.01	1.87±0.02
LG1 ^b	65	171	4.20	1.28	0.52±0.01	0.77±0.01	3.2	2.7

^a Errors represent SE of the means, propagated through subsequent calculations.

^b LG1 precipitation, Cl, porosity, and saturation data from White et al. (1998); errors represent SE of the means where the complete data was available.

Table 7. B1R regolith mineralogy by quantitative XRD^a

Depth (m)	Quartz (wt. %)	Hematite	Goethite	Kaolinite	Illite
0.04	36±2	0.10±0.01	4.6±0.2	36±2	10.6±0.5
0.2	38±2	0.13±0.01	5.9±0.3	38±2	11.9±0.6
0.4	37±2	0.060±0.003	6.4±0.3	35±2	15.4±0.8
0.6	54±3	0.047±0.002	3.7±0.2	20±1	23±1
0.8	28±1	0.43±0.02	20±1	20±1	27±1
1.3	40±2	0.96±0.05	4.8±0.2	41±2	12.5±0.6
2.3	40±2	0.64±0.03	3.9±0.2	42±2	13.6±0.7
3.1	37±2	1.4±0.1	3.6±0.2	41±2	14.0±0.7
3.5	40±2	0.35±0.02	12.4±0.6	22±1	25±1
3.7	57±3	0.096±0.005	2.5±0.1	20±1	20±1
5.0	45±2	0.73±0.04	3.1±0.2	34±2	16.6±0.8
5.6	42±2	1.1±0.1	3.2±0.2	38±2	10.5±0.5
5.6R ^b	58±3	0.93±0.05	3.0±0.1	26±1	7.4±0.4
6.2	31±2	2.1±0.1	4.0±0.2	52±3	5.1±0.3
6.2R	22±1	2.0±0.1	3.9±0.2	62±3	4.9±0.2
6.7	33±2	1.9±0.1	2.5±0.1	54±3	8.9±0.4
6.9	64±3	0.90±0.05	1.5±0.1	23±1	6.2±0.3
6.9R	79±4	0.41±0.02	1.8±0.1	11.0±0.6	5.6±0.3
7.4	69±3	0.71±0.04	3.6±0.2	15.2±0.8	10.3±0.5
7.6	63±3	1.2±0.1	1.7±0.1	21±1	7.7±0.4
7.6R	69±3	1.2±0.1	1.6±0.1	15.6±0.8	7.9±0.4
7.7	54±3	1.2±0.1	5.3±0.3	27±1	10.2±0.5
8.5	40±2	2.7±0.1	2.7±0.1	45±2	3.8±0.2
8.5R	31±2	2.9±0.1	2.1±0.1	54±3	4.5±0.2
8.9	21±1	3.6±0.2	3.0±0.1	61±3	7.5±0.4
9.3	14.0±0.7	3.3±0.2	4.1±0.2	65±3	5.1±0.3
9.3R	12.6±0.6	2.5±0.1	5.1±0.3	68±3	5.7±0.3
10.1	27±1	2.7±0.1	3.4±0.2	56±3	7.9±0.4
11.3	45±2	1.5±0.1	2.8±0.1	36±2	13.8±0.7
12.2	28±1	2.7±0.1	9.5±0.5	44±2	8.6±0.4
12.2R	22±1	3.3±0.2	3.6±0.2	62±3	4.7±0.2
13.1	50±3	2.0±0.1	2.5±0.1	31±2	11.9±0.6
14.3	25±1	2.9±0.1	5.1±0.3	52±3	13.7±0.7
14.9	24±1	3.8±0.2	3.7±0.2	56±3	8.2±0.4
14.9R	21±1	3.2±0.2	2.6±0.1	61±3	8.7±0.4
15.4	35±2	1.2±0.1	8.5±0.4	32±2	21±1
15.5	37±2	0.95±0.05	7.9±0.4	33±2	16.0±0.8
15.7	32±2	1.9±0.1	3.2±0.2	49±2	6.8±0.3
15.7R	19±1	2.0±0.1	3.4±0.2	64±3	5.6±0.3
15.8	33±2	2.6±0.1	2.9±0.1	48±2	11.0±0.5
15.9	37±2	3.3±0.2	3.5±0.2	41±2	5.3±0.3
15.9R	26±1	2.8±0.1	3.3±0.2	56±3	5.4±0.3

^a Error estimated at ± 5% of the measured value.^b Depths labeled R (shaded) are weathered clasts.

Table 8. B1S1 regolith mineralogy by quantitative XRD^a

Depth (m)	Quartz (wt. %)	Hematite	Goethite	Kaolinite	Illite	Chlorite	K-spar ^c	Plag ^b
0.6	21±1	1.6±0.1	5.2±0.3	61±3	11.1±0.6	-	-	-
0.9	30±2	1.7±0.1	3.7±0.2	52±3	12.2±0.6	-	-	-
1.2	28±1	1.8±0.1	3.8±0.2	56±3	10.7±0.5	-	-	-
1.5	29±1	1.3±0.1	3.3±0.2	56±3	9.9±0.5	-	-	-
1.8	17.5±0.9	2.1±0.1	2.9±0.1	67±3	10.7±0.5	-	-	-
2.7	18.2±0.9	2.3±0.1	3.4±0.2	61±3	14.9±0.7	-	-	-
3.1	11.7±0.6	2.4±0.1	3.4±0.2	69±3	13.9±0.7	-	-	-
3.7	18.8±0.9	2.2±0.1	3.0±0.2	60±3	16.2±0.8	-	-	-
4.3	24±1	1.4±0.1	3.7±0.2	57±3	14.3±0.7	-	-	-
4.9	18.1±0.9	1.9±0.1	3.0±0.1	22±3	15.2±0.8	-	-	-
5.5	18.7±0.9	2.0±0.1	2.9±0.1	61±3	15.2±0.8	-	-	-
6.4	19.0±0.9	2.0±0.1	2.4±0.1	59±3	17.2±0.9	-	-	-
7.0	16.7±0.8	1.6±0.1	3.9±0.2	59±3	18.7±0.9	-	-	-
7.6	19±1	1.6±0.1	3.5±0.2	55±3	21±1	-	-	-
8.2	14.3±0.7	2.1±0.1	3.2±0.2	62±3	18.4±0.9	-	-	-
8.5	25±1	0.99±0.05	2.3±0.1	55±3	17.3±0.9	-	-	-
9.0	33±2	0.49±0.02	1.9±0.1	44±2	11.0±0.6	7.2±0.4	2.4±0.1	-
9.0R ^c	74±4	0	1.3±0.1	7.1±0.4	3.2±0.2	7.7±0.4	6.3±0.3	-
9.3	22±1	0.48±0.02	2.0±0.1	46±2	12.8±0.6	12.1±0.6	4.2±0.2	-
9.3R	63±3	0	0.71±0.04	7.4±0.4	2.2±0.1	17.8±0.9	8.6±0.4	0.10±0.01

^a Error estimated at ± 5% of the measured value.^b K-spar = orthoclase, Plag = plagioclase^c Depths labelled R with shaded rows are weathered clasts from the given depth.

Table 9. Weathering gradients^a used to calculate weathering rates and fluxes in Eq. 8-11.

	Rio Icacos	Bisley			
	LG1	B1R	B1S1	B1S2	B1S4
<i>Solid-state weathering gradients b_s ($m\ kg\ mol^{-1}$)^b</i>					
Mg (regolith)	1.12±0.02 (1.0)	-	46±6 (0.72)	5.9±0.5 (0.82)	3.5±0.6 (0.64)
Mg (chlorite)	-	-	6±1 (0.69)	-	-
Si	-	-	2.6±0.7 (0.67)	1.1±0.5 (0.49)	0.4±0.1 (0.99)
K	17±2 (0.59)	-	72±8 (0.57)	-	4.8±0.5 (0.95)
P	44±8 (0.75)	-	110±20 (0.93)	-	-
Kaolinite	-	-	7.5±0.6 (0.76)	-	-
Illite	-	-	30±10 (0.95)	-	-
<i>Solute weathering gradients b_f ($m\ L\ mol^{-1}$)^c</i>					
Mg	1.1x10 ⁵ (0.48)	1.1x10 ⁶ ±7x10 ⁵ (0.63)	7x10 ⁵ ±4x10 ⁵ (0.61)	-	-
Si	3.6x10 ⁴ (0.74)	3.3x10 ⁴ ±3x10 ³ (0.56)	5.8x10 ⁴ ±3x10 ³ (0.99)	-	-
K	2.0x10 ⁵ (0.82)	-	-	-	-
<i>Depth range and Δz (m)^d</i>					
Solid-state Mg (regolith)	4.6-4.9 (0.3)	-	1.2-9.3 (8.1)	0.9-2.7 (1.8)	0.15-0.9 (0.6)
Solid-state Mg (chlorite)	-	-	8.2-9.3 (1.1)	-	-
Solid-state Si	-	-	1.8-9.3 (7.5)	0.9-2.7 (1.8)	0.15-0.9 (0.6)
Solid-state K	0.15-4.9 (4.8)	-	1.8-9.3 (7.5)	-	0.15-0.9 (0.6)
Solid-state P	4.0-4.9 (0.8)	-	8.2-9.3 (1.1)	-	-
Kaolinite	-	-	0.9-4.6 (4.3)	-	-
Illite	-	-	0.6-7.6 (7.0)	-	-
Solute Mg	1.2-8.5 (7.3)	1.2-16.0 (14.8)	1.2-9.3 (8.1)	-	-
Solute Si	1.2-8.5 (7.3)	1.5-16.0 (14.5)	1.8-9.3 (7.5)	-	-
Solute K	1.2-8.5 (7.3)	-	-	-	-

^a Errors reflect detection limits and SE of averages fully propagated through the calculations.

^b Solid state gradients are linear regressions over normalised concentrations (Figures 7-8) and R² values are given in parentheses. Dashes for elemental gradients indicate absence of a measurable gradient for the given element in the given profile. Kaolinite and illite gradients are only shown for B1S1 because mineralogical analysis was not done for B1S(2-4), gradients were not detected for these minerals in B1R and Rio Icacos contains a different mineral assemblage.

^c Solute gradients (Figure 2) only given for Bisley ridgetop profiles (B1R and B1S1) as the influence of lateral subsurface solute transport cannot be ruled out for slope sites B1S(2-4). Weathering solute concentrations of K were below detection at most depths in Bisley pore waters. Rio Icacos solute gradients are from White (2002) for Mg and K and Schulz and White (1999) for Si.

^d Depth ranges over which the weathering gradients were determined with Δz in parentheses.

Table 10. Weathering rates and fluxes^a

	Río Icacos	Bisley			
	LG1	B1R	B1S1	B1S2	B1S4
<i>Solid-state weathering fluxes, Q_{LT}: $\log(\text{mol m}^{-2}\text{s}^{-1})$</i>					
Mg	-7.8 (-8.0 to -7.7)	-	-4.5 (-4.6 to -4.4)	-5.1 (-5.2 to -5.1)	-5.3 (-5.4 to -5.2)
Si	-	-	-4.2 (-4.3 to -4.0)	-4.4 (-4.7 to -4.2)	-4.3 (-4.5 to -4.1)
K	-9.0 (-9.2 to -8.9)	-	-5.5 (-5.6 to -5.5)	-	-5.4 (-5.5 to -5.3)
P	-10.3 (-10.5 to -10.1)	-	-6.6 (-6.7 to -6.5)	-	-
<i>Solute weathering fluxes, Q_{ST}: $\log(\text{mol m}^{-2}\text{s}^{-1})^b$</i>					
Mg	-8.7	-9.4 (-9.9 to -9.1)	-9.5 (-9.8 to -9.3)	-	-
Si	-8.2	-7.9 (-8.0 to -7.8)	-8.4 (-8.5 to -8.4)	-	-
K	-8.9	-	-	-	-
<i>Solute watershed-averaged weathering fluxes: $\log(\text{mol m}^{-2}\text{s}^{-1})^c$</i>					
	<u>Río Icacos</u>	<u>Río Mameyes</u>			
Mg	-8.5	-8.4			
Si	-7.6	-7.6			
K	-8.8	-8.9			
<i>Mineral weathering rates, R_{LT}: $\log(\text{mol m}^{-2}\text{s}^{-1})^d$</i>					
Chlorite	-	-	-13.1 (-13.2 to -13.0)	-	-
Kaolinite	-	-	-13.4 (-13.5 to -13.3)	-	-
Illite	-	-	-13.7 (-13.9 to -13.5)	-	-

^a Calculated from Eqns. 8-11 using parameters given in Table 9 and in the text. Ranges, shown in parentheses, reflect \pm errors fully propagated through the calculations.

^b Solute weathering fluxes only given for ridgetop profiles (LG1, B1R, B1S1) as the influence of lateral subsurface solute transport cannot be ruled out for the slope sites B1S(2-4). Río Icacos Mg and K weathering fluxes were calculated from Eqn. 11 using gradients calculated by White (2002) and Schulz and White (1999) and q_h and Γ values (Table 6).

^c Solute watershed-averaged weathering fluxes from Stallard (2012), determined from riverine and atmospheric fluxes over 1991-2005 in the Río Icacos and Río Mameyes (which the Bisley streams feed into).

^d Mineral weathering rates are only shown for B1S1 because mineralogical analysis was not done for B1S(2-4), gradients were not detected for these minerals in B1R and Río Icacos contains a different mineral assemblage.

Figure 1
[Click here to download high resolution image](#)

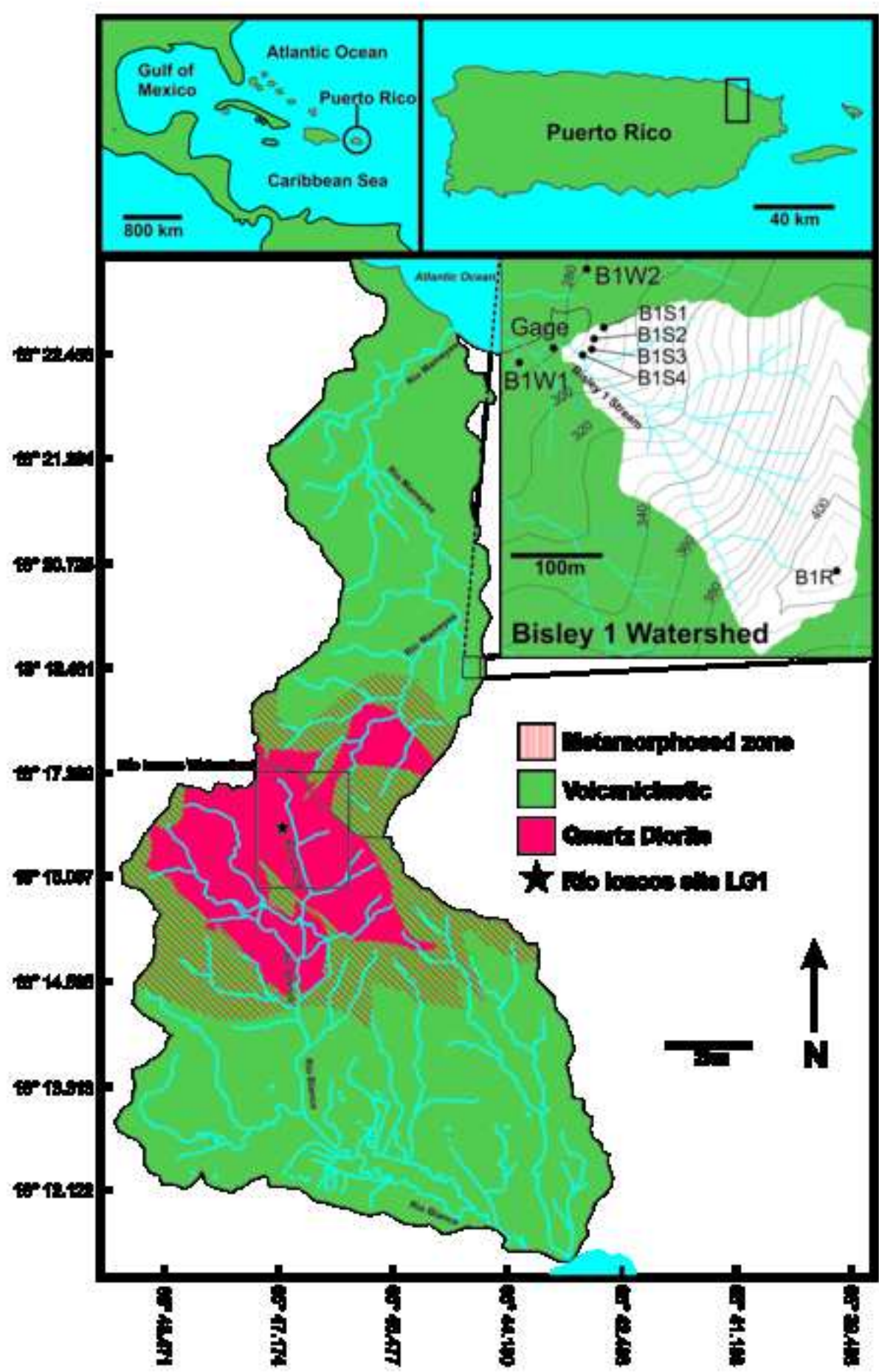


Figure 2
[Click here to download high resolution image](#)

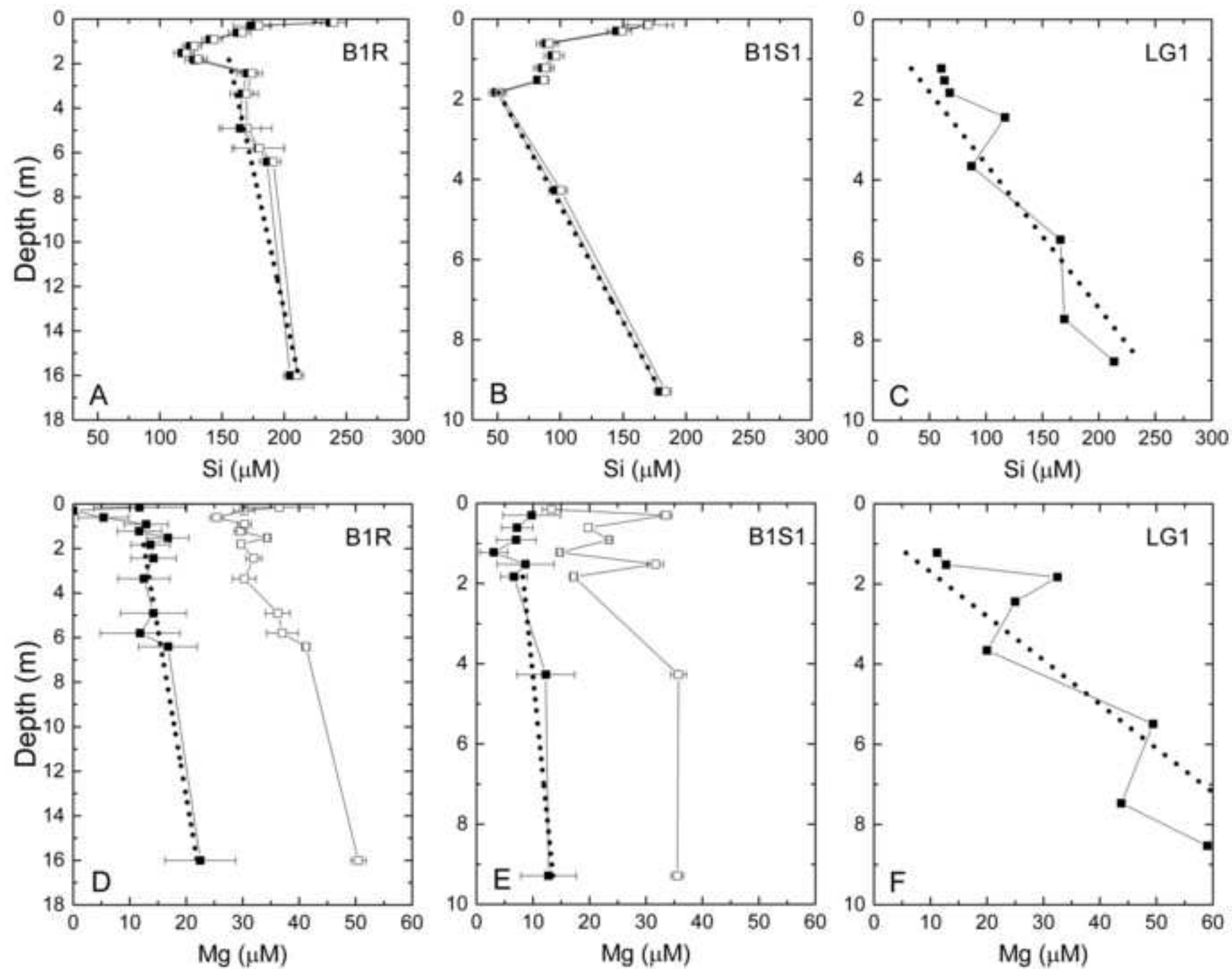


Figure 3
[Click here to download high resolution image](#)

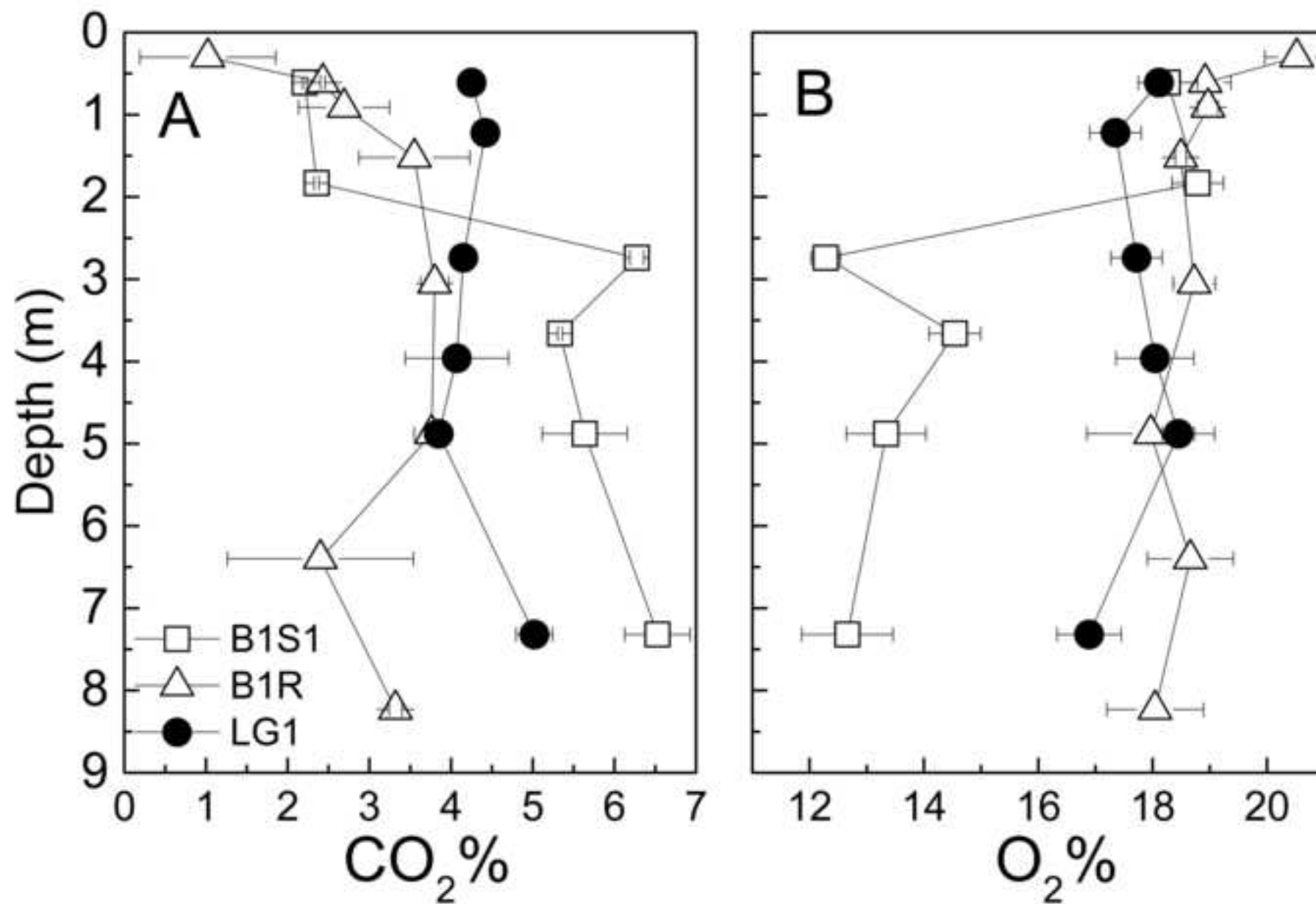


Figure 4
[Click here to download high resolution image](#)

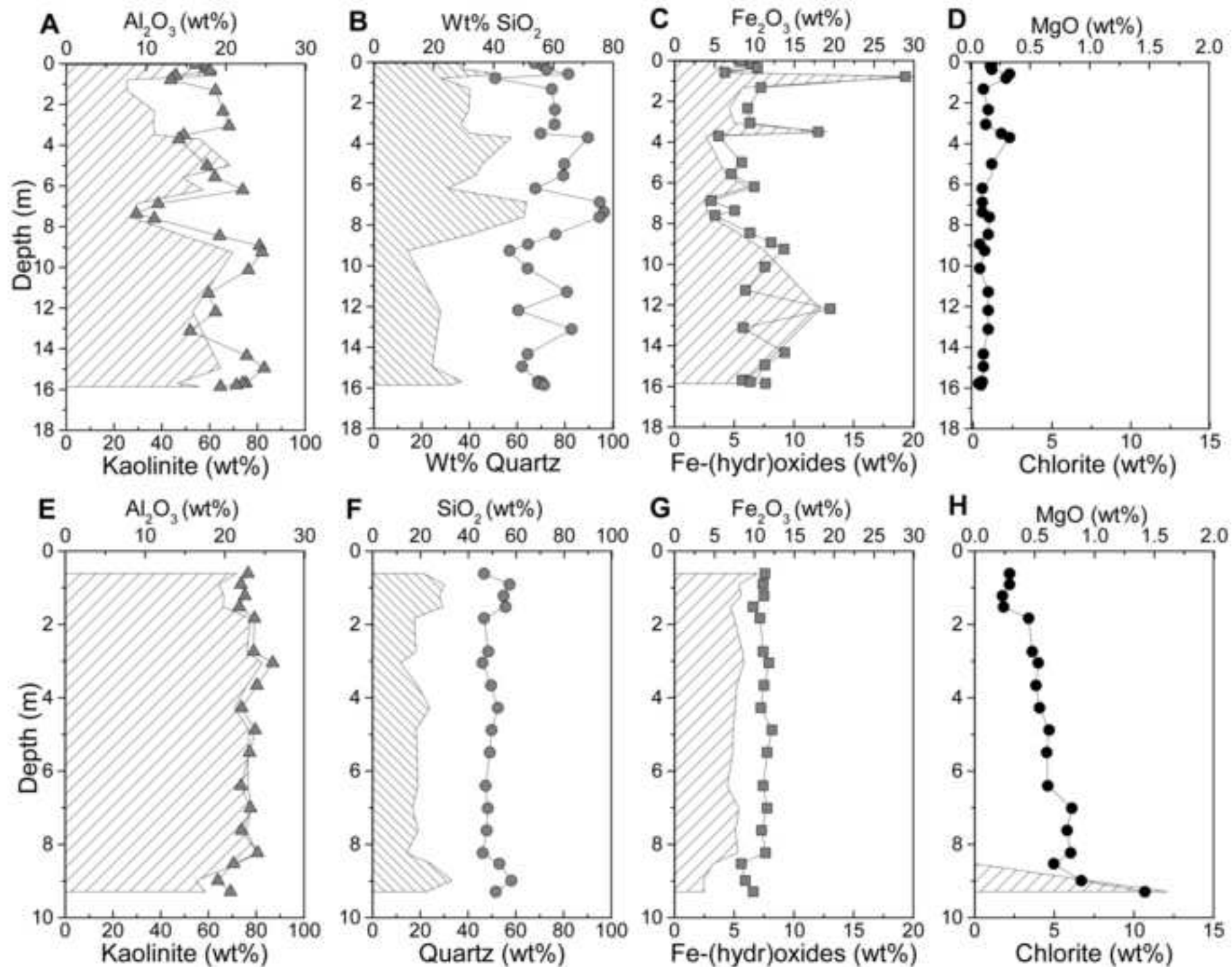


Figure 5
[Click here to download high resolution image](#)

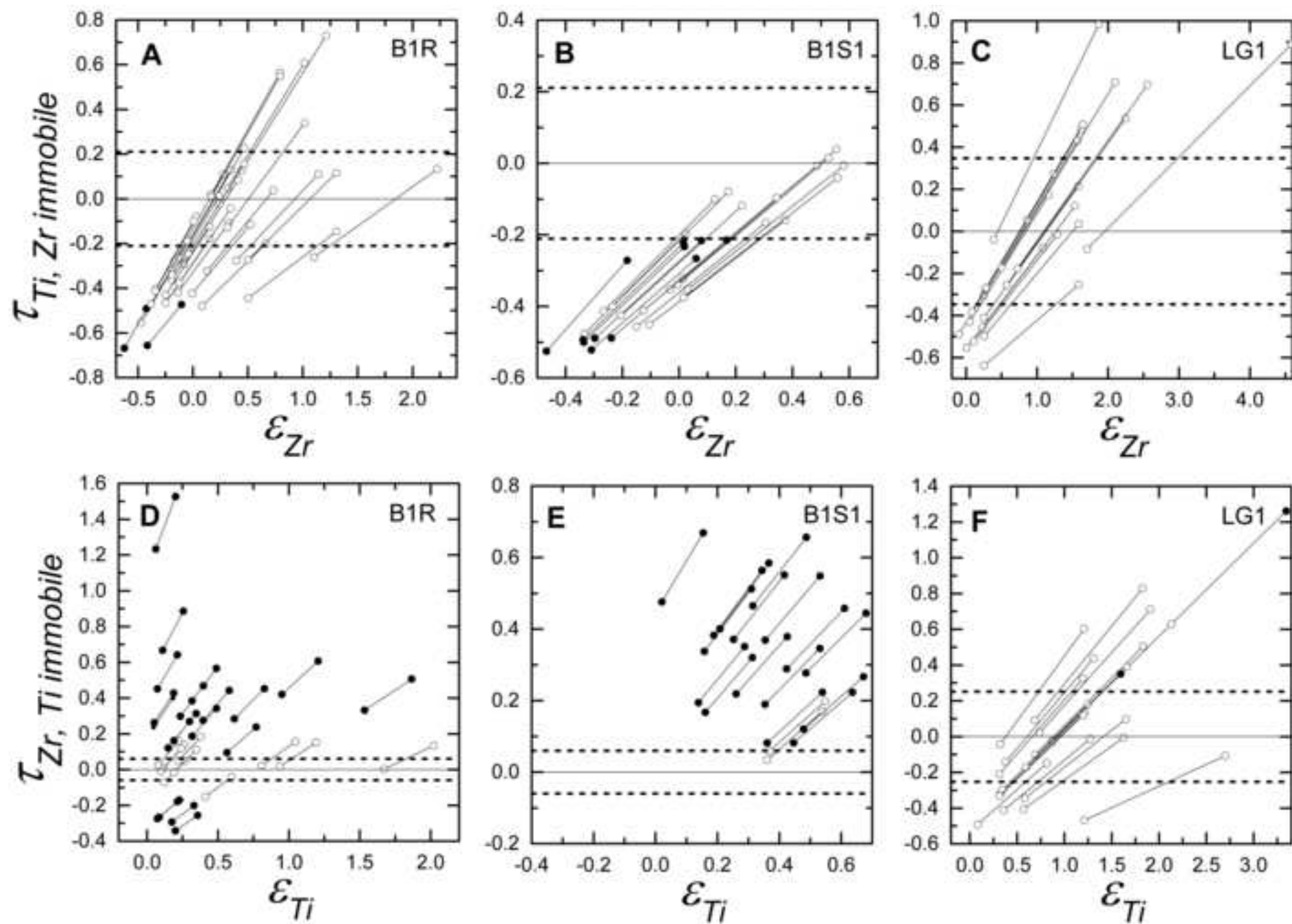


Figure 6

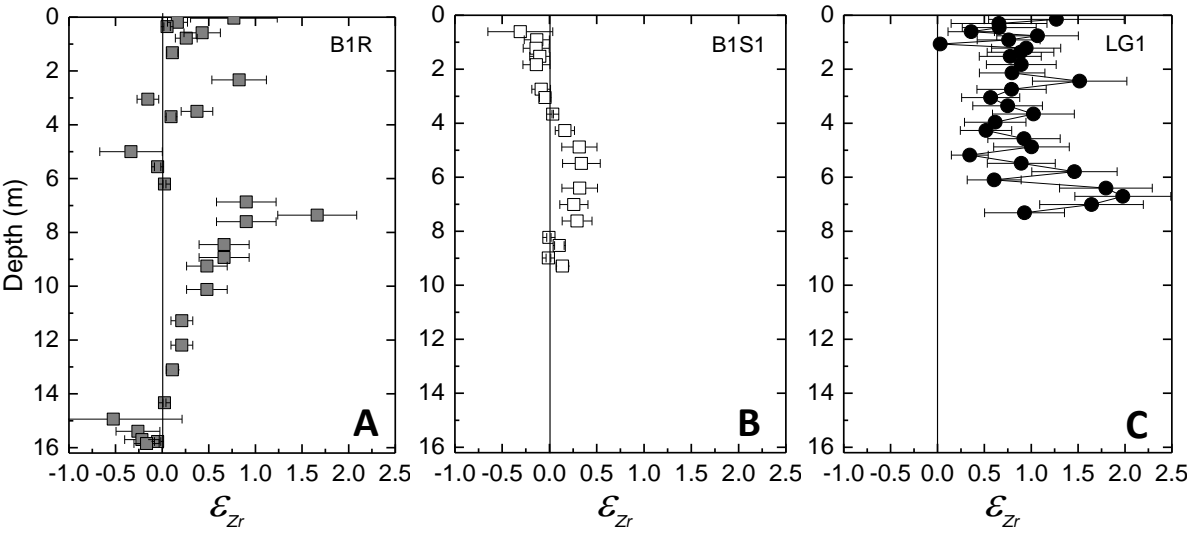


Figure 7

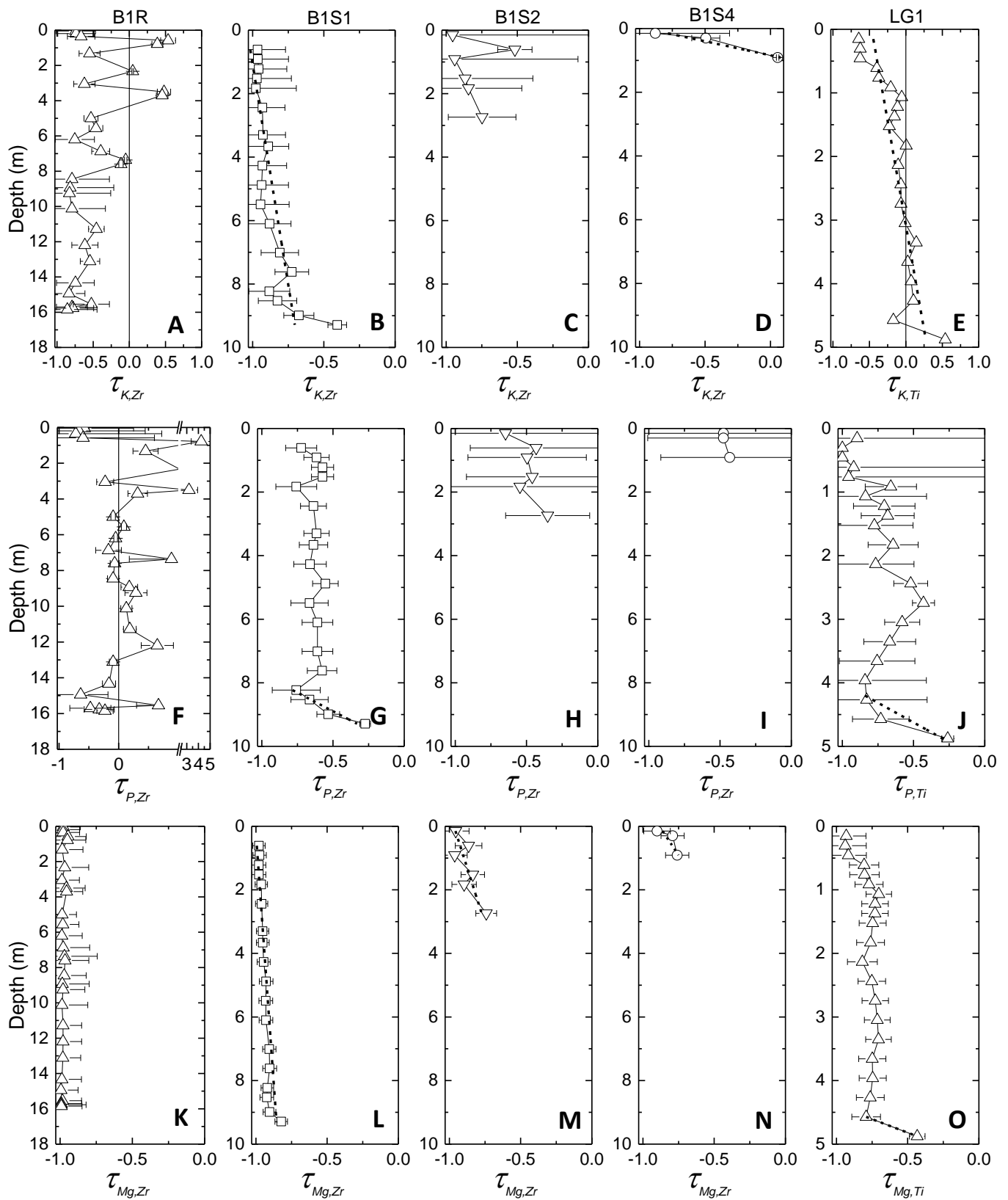


Figure 8

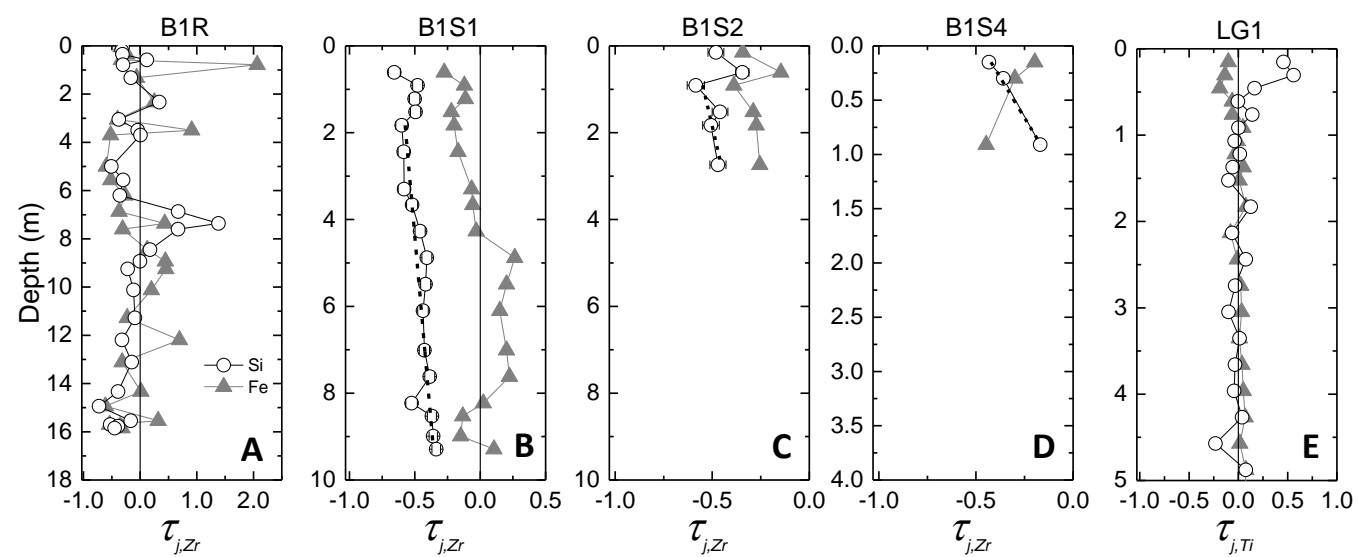


Figure 9

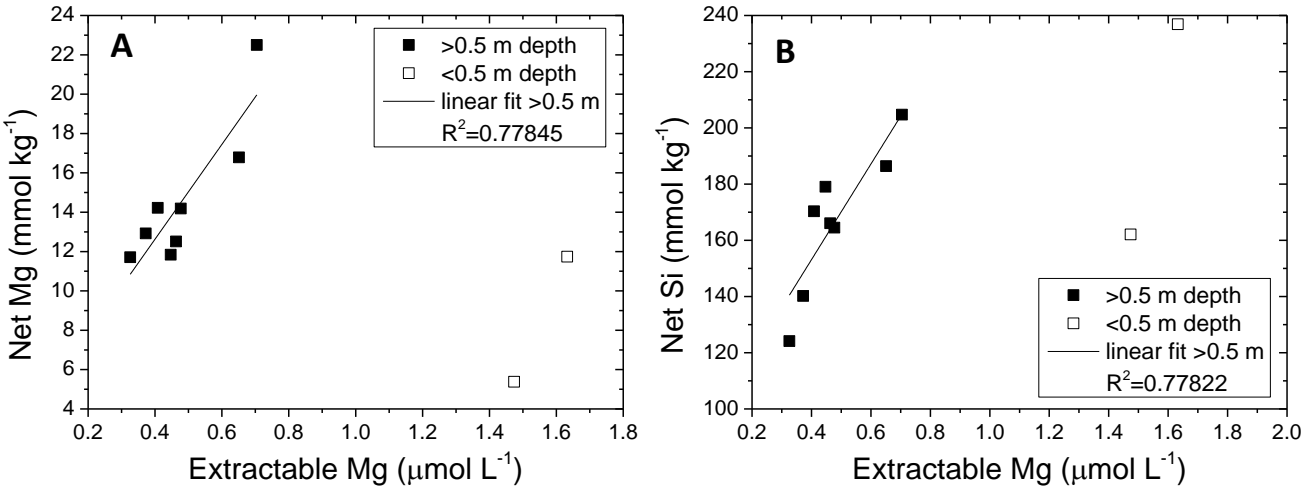


Figure 10

